Supplementary Information

Photonically Active Bowtie Nanoassemblies with Chirality Continuum

Prashant Kumar[1,2], Thi Vo[1,2], Minjeong Cha[1,2], Anastasia Visheratina[1,2], Ji-Young Kim[1,2], Wenqian Xu[3], Jonathan Schwartz[4], Alexander Simon[1], Daniel Katz[1], Emanuele Marino[5], Wonjin Choi[1], Si Chen[3], Christopher Murray[5], Robert Hovden[4], Sharon Glotzer[1,2,4*], Nicholas A. Kotov[1,2,4*].

[1]Department of Chemical Engineering, University of Michigan, Ann Arbor, MI, 48109, USA;
[2]Biointerfaces Institute, University of Michigan, Ann Arbor, MI, 48109, USA;
[3]X-ray Science Division, Advanced Photon Source, Argonne National Laboratory, Lemont, IL 60439, USA.
[4]Department of Materials Science and Engineering, University of Michigan, Ann Arbor, MI, 48109, USA;
[5]Department of Chemistry, University of Pennsylvania, Philadelphia, PA 19104, USA;

Corresponding authors: sglotzer@umich.edu, kotov@umich.edu

METHODS

XRD data acquisition.

Preliminary structure evaluation was done using powder X-ray diffraction data acquired from a Rigaku Smartlab diffractometer with a source of Cu-Kα at 40 kV voltage and 44 mA current (λ = 1.54059 Å). The optics included a K-beta filter and Soller slit. The diffractometer was operated in Bragg-Bentano configuration, and the signal was collected on Scintillation Counter (SC-70), D/tex ultra 250 high speed silicon strip 1D. Data was acquired from 5º to 75º with a step size of 0.01º. Synchrotron X-ray powder diffraction data (λ = 0.45192 Å) was collected at Beamline 17-BM at the Advanced Photon Source at the Argonne National lab. Freeze dried powder sample of *L-/D-/rac*-bowties was loaded in a 1.0 mm diameter Kapton capillary tube, which was then measured using a VAREX XRD 4343CT amorphous silicon area detector in the Debye-Scherrer geometry. The resulting 2D diffraction pattern was integrated using the GSAS-II software[1] into an 1D pattern of intensity versus 2θ, which was then used for structure solution and refinement.

XRD structure solution and refinement

Structure solution was performed with the TOPAS software on the synchrotron powder XRD data. A total of 31 low angle peaks were used for indexing. The result indicated an orthorhombic unit cell with three edges of around 20.48 Å, 9.94 Å and 5.05 Å. Considering the chirality of the bowtie morphology of the material observed under electron microscope, the spaces group should be one of the Sohncke groups that have only symmetry operations of first kind. The extinction conditions

of the space group $P2_12_12_1$ shows the best match with the observed PXRD data, though $P2_12_12$ was also tried in the structure solution process. Unit cell parameters, sample displacement, background and profile parameters were refined by Pawley refinement and fixed in the subsequent structure solution process, where the simulated annealing method built in TOPAS was used. The L-CST was modeled as rigid body with flexibilities on bond angles and torsion angles. Cd was treated as a free atom. Chemical analysis based on the EDX result and the titration measurements pointed to a Cd/S ratio of 1 to 2, equal to 1 Cd per L-CST molecule. Considering the cell volume, 1 Cd atom and 1 L-CST were employed per asymmetric unit. Hydrogen atoms were not modeled. The correct structure solution did not appear until after more than 50 attempts, mainly due to the low resolution of the data, which has a minimum d-space of 1.6 Å and shows severe peak overlap at below 2.5 Å as a result of the nanosized particles of the sample, as well as the low sensitivity of the data to different configurations of L-CST. After the correct structure model emerged, Rietveld refinement was performed. The atomic displacement parameter (ADP) of all the atoms in L-CST were constraint to be the same, while the ADP of Cd was refined independently. Other than the ADPs, fractional coordinates of the Cd site, translation and rotation of the L-CST rigid body, bond angles and torsion angles within the rigid body, unit cell parameters, the sample displacement parameter and the background were also refined. The background was modeled by Chebyshev polynomial of 3 coefficients. In the final cycle of refinement generating the crystallographic information file (CIF), the two ADP parameters, Cd atomic fractional coordinates, the L-CST rigid body translation, cell parameters and sample displacement were refined. Including other parameters in the final cycle did not visibly change the structure or the quality of the fitting, but greatly enlarged calculated errors of fractional coordinates of many atoms. This is due to the resolution of the diffraction data and ultimately attributed to the nanostructured nature of the material.

LIDAR measurements

The customized bench-top polarization LIDAR system was used for the measurement of the polarization effect of scattering light from the deposited *L*- and *D*-type bowtie particles. As shown in the scheme, 5 ns and 25 kHz pulsed 1550 nm laser (Bktel) was activated by pulse generator (Quantum composer 9200) and powered by 5 V/3 A power supply. The collimated laser beam can be modulated to any polarization state, linear to circular, by passing through the combination of a linear polarizer and a quarter wave plate. The polarized incident beam is directed by motorized X-Y galvo mirror steerer (Thorlabs) to scan the sample in the X-Y space. The servomotor is controlled by an NI DAQ instrument with 10 points/sec. The scattered light from the sample is collected with the large beam collecting lens system and detected by 400 MHz InGaAs photodetector (Femto) connected with the oscilloscope (picoscope) to capture the intensity and time of flight of pulse that hits the samples to capture the full 3D point cloud data. The pulse generator, DAQ motor controller, and intensity detecting oscilloscope are synchronized using in-lab written MATLAB code to save the XYZ 3D-coordinates of scanned area and its polarized intensity at each point.

Firstly, to measure the linear dichroism effect of the sample from the scattered light at 1550 nm, the linear polarizer at the incident beam needs to be set to 0 ° and 90 ° leaving the quarter wave plate at “off” state. At every scan point, the value of *LD effect* would be measured to see if there is linear difference in *L*- and *D*-bowties.

$$Linear\ Dichroism\ (LD)\ scattering\ effect = \ Intensity(0\ °) - Intensity(90\ °)$$

Similarly, the circular dichroism would be measured by the following equation and the linear polarizer at the incident beam will be set to 0 ° and 90 ° , for the LCP and RCP respectively, leaving the quarter wave plate at "on" state (fast axis is 45 ° off from the 0 °).

$$Circular\ Dichroism\ (CD)\ scattering\ effect = \ Intensity(LCP) - Intensity(RCP)$$

If the sample is *L*-type, it should absorb LCP light more than RCP, as a result, RCP scattering would be dominant ($CD\ scattering\ effect < 0$) . For the *D*-type sample, vice versa, and the $CD\ scattering\ effect > 0$.

Simulation of Bowtie Growth

Coarse-Grained Modeling of Bowtie Growth. Structural analysis using XRD data suggests multiple possible solutions (i.e. structures) that can fit the crystallography results. As such, rather than directly mapping one particular structure to a coarse-grained model, we pick relevant features that are consistent across the possible solutions to construct a generalized building block that can reproduce the assembly behavior in our Monte Carlo growth simulations. The key features we chose to adapt are (**SI Fig. 11**): 1). Building blocks are rectangular prism-like and flat with rough dimensions of 20 x 10 x 5 as suggested from XRD. 2). H-bonding sites decorate the two largest and two smallest facets to reflect the bonding between the –COOH and $–NH_2$ groups. 3). The two intermediate facets exhibit specific, directional interaction to capture the disulfide bridge formation intrinsic to the CST used in the experimental system. These interactions sites only interact with themselves. For ease of notation, we refer to these sites as sulfur linkage sites. 4). Building block exhibit a slight shear on one facet to enforce chirality of L-CST vs R-CST. 5). Isotropic charge-charge repulsion between Cd^{2+} atoms embedded inside the rectangular building block. Each building block has a scaled net charge of +1 to reflect a net charge on building blocks indicated by experiemtanl zeta-potential measurements. This choice additionally builds in charge-driven, self-limiting behaviors. 6). All other surface sites not defined by h-bonding or sulfur linkage exhibit steric repulsion.

Computing potentials of mean force (PMF) between our coarsed grained building blocks reveal that our proposed model exhibit the features necessary to capture the heirarchy of structural formation observed in experiments: that is, chains assembling into nanosheets that then stack to ultimately form the observed bowtie structures (**Fig. 2g,h**). PMFs computed for a mix of *L*-CST and *R*-CST reveals a reduction of tendency in hiearchical structural formation, driving the transition from bowtie to pancake structure. We then employ the computed PMFs to perform Monte Carlo growth simulations to confirm the formation of both bowtie and pancake morphologies (**Fig. 2i,j**).

Modeling of Bowtie assembly. For the system of interest, there are three possible choices for CST enantiomers in the helical chains from Cd_2CST_2 units producing one racemic and two homochiral versions that can be abbreviated as LCD, LCL, and DCD. LCL and DCD are equal in energy when they do not interact with other chiral species. However, LCD differs from LCL (or DCD) by an energy quantity ΔU. Thus one can describe the probability of their formation in the mixture of CST enantiomers with different χ by writing the partition function Z as $Z = 1 + e^{-\beta\Delta U}$, where $\beta = 1/k_bT$. The probability P_{LCD} of forming the LCD nanocluster is directly related to enantiomeric excess of CST, χ, used in experiments. Using classical statistical mechanics, we can equate the Boltzmann weighted energy difference to P_{LCD} to give

$$1 - \frac{1+\chi}{2+\chi} = \frac{e^{-\beta\Delta U}}{1+e^{-\beta\Delta U}} \tag{1}$$

Solving for ΔU gives the energy difference of LCD relative to LCL (or DCD) explicitly in terms of χ to be $\beta\Delta U \sim \ln(1+\chi)$. The average twist angle, given an excess fraction of enantiomer, can then be determined as $\langle\cos(\theta(\chi))\rangle = \int \cos(\theta(\chi))\, P(\theta(\chi))d\theta$. For our system, there are only three possible choices for CST enantiomers – LCD, LCL, and DCD – enabling us to convert the integral to a sum over all 3 enantiomeric types.

$$\langle\cos(\theta(\chi))\rangle = \sum_{i\,\epsilon\,\{LCL,LCD,DCD\}} \cos(\theta_i(\chi))\, P(\theta_i(\chi)) \tag{2}$$

Plugging in $P(\theta(\chi))$ for each respective state and noting that $P_{LCL} = P_{DCD}$, we get

$$\begin{aligned}\langle\cos(\theta(\chi))\rangle = Z^{-1}\{&(1+\chi)^{-1}\cos(\theta_{LCD}(\chi)) \\ &+ 2^{-1}[\cos(\theta_{LCL}(\chi)) + \cos(\theta_{DCD}(\chi))]\}\end{aligned} \tag{3}$$

Let the angle between LCL be θ_c and noting that LCL and DCD are mirror images (i.e. $\theta_{LCL} = -\theta_{DCD}$) gives

$$\langle\cos(\theta(\chi))\rangle = Z^{-1}\{(1+\chi)^{-1}\cos(\theta_{LCD}(\chi)) + \chi\cos\theta_c\} \tag{4}$$

Additionally, we approximate the angle for LCD to be small (to reflect the "pancake" motif). Perturbation of $\cos(\theta_{LCD}(\chi))$ about a small θ_{LCD} and taking the first term gives

$$\langle\cos(\theta(\chi))\rangle = Z^{-1}\{(1+\chi)^{-1} + \chi\cos\theta_c\} \tag{5}$$

From earlier, we know $Z = [2+\chi][1+\chi]^{-1}$, plugging Z into Eq. 5 gives

$$\langle\cos(\theta(\chi))\rangle = \frac{\chi(1+\chi)\cos\theta_c + 1}{2+\chi} \tag{6}$$

We then employ Eq. 6 to predict the relevant dimensions of the resulting bowtie particles. The growth directions reflect end-to-end or top-bottom stacking of the coarse-grained building blocks. As such, a scaling model approach to computing the gain in surface area as a function of increasing number of nanoclusters can be written as follows. (**SI Fig. 30**)

$$A_{n1} \sim L^2 \left[\frac{1 + (n-1)(P_1\gamma_2 + P_2)}{n} + 2\alpha + 2\alpha(n-1)(P_1\gamma_1 y_2 + P_2) + (n-1)P_1(\gamma_2 - 1)^2 \right] \tag{7a}$$

$$A_{n2} \sim L^2[1 + (n-1)(P_1\gamma_1^2 + P_2) + \alpha + \alpha n(P_1\gamma_1 y_2 + P_2) + \alpha(n-1)P_1(\gamma_2 - 1)^2] \tag{7b}$$

where A_{n1} and A_{n2} are the areas for edge-edge and top-bottom stacking directions respectively. L is the characteristic length of the nanocluster along its long axis, α is the aspect ratio measuring the amount of nanocluster elongation, n is the number of nanoclusters in the assembly, and γ_1 and γ_2 are the local curvature of the nanoclusters along the long and short direction, respectively, that enables generalization of our model to differently shaped building blocks. P_1 and P_2 are defined as

$$P_1 = P(LCL)P(LCD) = (2Z)^{-1}(2 + \chi)^{-1} \tag{8a}$$

$$P_2 = P(LCL)P(LCL) = (2Z)^{-2} \tag{8b}$$

P_1 and P_2 can thus be interpreted as the probability of an LCL (or DCD) nanocluster adding to a LCD or LCL (DCD) surface nanocluster of the growing bowtie, respectively. The total surface area of the growing bowtie is then simply

$$A_T = P_{d1}A_{n1} + (P_{d2} + P_{d3})A_{n2} \tag{9}$$

where P_{di} is the Boltzmann weighted growth probability in the i^{th} direction using the computed PMFs. Results from simulation suggests that when electrostatics repulsion dominates over H-bonding, the bowtie particles cease to grow, creating a self-limiting size effect. Here, we assume that each nanocluster gains 4 hydrogen bond upon incorporation into the growing bowtie. Additionally, the Cd^{2+} moieties within each nanocluster also contributes to local coordination as well as repulsion with other Cd^{2+} moieties on neighboring nanoclusters. These effects are incorporated into the computed PMFs (P_{di}) employed in Eq. 9. We can explicitly compute the size of the self-limiting assembly by equating the electrostatic repulsion with attraction from short-range forces. In other words, we write $E_{Hbond} \sim E_{charge}$. Hydrogen bonds are generally on the order of kT, as such we take E_{Hbond} to be of order unity ($E_{Hbond} \sim 1$). E_{charge} is approximated to be the total surface charge Q of the bowtie acting on the closest point on the surface of the growing front relative to the center of the bowtie. We define the distance to this proximal surface point as R, allowing us to write $E_{charge} \sim Q/R$. When $E_{Hbond} \sim E_{charge}$, this distance R becomes the self-limiting size of the particle R^*. The total surface charge is simply the charge of the composite cluster distributed over the total surface area of the growing bowtie: $Q \sim nqA_T^{-1}$. As such, we have

$1 \sim (nA_T^{-1})qR^{-1}$, where q is the charge of a nanocluster (taken to be of order unity). Rearranging for R^* and taking the limit of A_T for $n \gg 1$ to reflect experimental observations that bowtie dimensions are orders of magnitude large than their constitutive building blocks result in Eq. 10.

$$\begin{aligned} R^* \sim nA_T^{-1} \sim n\{&P_1[P_{d1}\gamma_2 + (P_{d2} + P_{d3})\gamma_1^2] + P_2 \\ &+ \alpha(2P_{d1} + P_{d2} + P_{d3})(P_1\gamma_1\gamma_2 + P_2) \\ &+ P_1[P_{d1}(\gamma_2 - 1)^2 + \alpha(P_{d2} + P_{d3})(\gamma_1 - 1)]\}^{-1} \end{aligned} \tag{10}$$

Eq. 10 defines the shortest radial distance from the center to the bowtie's surface. Therefore, the thickness of the bowtie is $R_t \sim R^*\langle\cos\theta\rangle$. Similarly, the width is $R_w \sim R^*\langle\sin\theta\rangle^{-1}$ and length is $R_l \sim R_w\langle\sin\theta\rangle^{-1}$. Comparison of theoretical prediction with both experiments and simulations yields the results shown in Fig. SS2. Lastly, we can explicitly determine the number of nanoclusters n^* in the self-limiting bowtie via $\partial R^*/\partial n = 0$ and solving for n. Doing so gives

$$n^* \sim \{\Gamma_1 + \Gamma_2\}\{\partial_n A_{T,1} + \partial_n A_{T,2}\}^{-1} \tag{11}$$

where

$$\begin{aligned} \Gamma_1 &= P_{d1}\{1 - P_1[\gamma_1 + (\gamma_2 - 1)^2] + P_2 + 2\alpha[1 - P_1\gamma_1\gamma_2 - P_2]\} \\ \Gamma_2 &= \{P_{d2} + P_{d3}\}\{1 - P_1\gamma_2^2 - P_2 - \alpha P_1\gamma_1\} \\ \partial_n A_{T,1} &= P_{d1}[2\alpha(P_1\gamma_1\gamma_2 + P_2) + P_1(\gamma_2 - 1) + P_1\gamma_2 P_2] \\ \partial_n A_{T,2} &= \{P_{d2} + P_{d3}\}\{\alpha[P_1(\gamma_1\gamma_2 + \gamma_1 - 1) + P_2] + P_1\gamma_1^2 + P_2\} \end{aligned}$$

Extension to Incomplete Nanocluster Formation. The above derivations assumes that only perfect Cd_2CST_2 nanoclusters form during the assembly process. Here, we extend the theoretical construction to account for the possible formation of incomplete nanoclusters. More specifically, we consider the existence of 3 types of nanoclusters – Cd_2CST_2, Cd_2CST_1, and Cd_1CST_1. We first define the fraction of incomplete cluster in the system as δ. Rather than having a single P_{LCD} to balance with the Boltzmann weighting (Eq. 1), we now have 6 probabilities corresponding to the each of Cd_2CST_2, Cd_2CST_1, and Cd_1CST_1 for both LCL (DCD) and LCD formations. Similar to Eq. 1, the reference state is taken to be that of P_{LCL}, reducing the problem to 5 coupled equations of the following form

$$\delta^2 g(\chi) = Z^{-1}e^{-\beta\Delta U_2} \tag{12a}$$

$$\delta g(\chi) = Z^{-1}e^{-\beta\Delta U_3} \tag{12b}$$

$$f(\chi) = Z^{-1}e^{-\beta\Delta U_4} \tag{12c}$$

$$\delta f(\chi) = Z^{-1}e^{-\beta\Delta U_5} \tag{12d}$$

$$\delta^2 f(\chi) = Z^{-1}e^{-\beta\Delta U_6} \tag{12e}$$

where ΔU_2, ΔU_3, ΔU_4, ΔU_5, and ΔU_6 are the energy difference a perfect Cd_2CST_2 formation and Cd_1CST_1 (LCL), Cd_2CST_1 (LCL), Cd_2CST_2 (LCD), Cd_2CST_1 (LCD), and Cd_1CST_1 (LCD), respectively. The functions Z, $f(\chi)$, and $g(\chi)$ are defined such that:

$$Z = 1 + \sum_{i=2}^{6} e^{-\beta \Delta U_i}$$

$$g(\chi) = \left(\frac{1+\chi}{2+\chi}\right)\left[\frac{3}{4} + \frac{1}{4}\,(2\delta+1)^2\right]^{-1}$$

$$f(\chi) = \left(1 - \frac{1+\chi}{2+\chi}\right)\left[\frac{3}{4} + \frac{1}{4}\,(2\delta+1)^2\right]^{-1}$$

Solving Eq. 12 gives the following set of general solutions

$$\beta \Delta U_i = -\ln\left([1 + Z_{i+1}]\frac{x_i}{1-x_i}\right)$$

$$x_2 = \delta^2 g(\chi) \tag{13a}$$

$$x_3 = \frac{1}{\delta}\frac{x_2}{1-x_2} \tag{13b}$$

$$x_4 = f(\chi)(\delta x_3 + 1)\left(1 - \frac{x_3}{1-x_3}\right) \tag{13c}$$

$$x_5 = \delta x_4\left(1 + \frac{x_4}{1-x_4}\right) \tag{13d}$$

$$x_6 = \delta x_5\left(1 + \frac{x_5}{1-x_5}\right) \tag{13e}$$

Eq. 13 can now be plugged into the governing equation for the twist angle (Eq. 2), but now the sum is over 6 enantiomeric states instead of 3. Solution for the twist angle directly plugs into subsequently equations to predict the dimensions of bowties outline in the previous section. Comparison of Monte Carlo growth simulation results incorporating the incomplete clusters with the theoretical extensions are shown in **SI Fig. 27** (δ is mapped to experimental Cys/Cd ratio).

Osipov-Pickup-Dunmur chirality measure (OPD) calculations

Bowties parameters (length, width, thickness, twist angle) were extracted from the experimental data. Osipov-Pickup-Dunmur chirality measure (OPD)[2] was calculated using the previously described method [3] that uses the eight secondary center of masses extracted from different bowtie 3D models built with geometric parameters presented above. The center of each bowtie, which will be referred to as the primary center of mass, was placed at the (0,0,0) point of the Cartesian coordinate system. Bowtie length was aligned along *x*-axis and width along *y*-axis. Then, the bowtie was sectioned into eight pieces according to octants of the Cartesian system. Coordinates from their center of masses of the eight sections, referred to as secondary centers of masses, have been calculated. Using the coordinates of the eight secondary center of masses, OPD for all of the structures above were calculated.

The tensor gives rise to two universal chirality indices; the first giving information about absolute chirality, and the second about the anisotropy chirality, *i.e.,* the degree of chirality in different spatial directions. The pseudoscalar behavior of chiral molecule can be described by the gyration tensor *G*,

$$\mathbf{G}=\int d\mathbf{r}_1 d\mathbf{r}_2 d\mathbf{r}_3 d\mathbf{r}_4 \rho(\mathbf{r}_1)\rho(\mathbf{r}_2)\rho(\mathbf{r}_3)\rho(\mathbf{r}_4) \times \frac{[(\mathbf{r}_{12}\times\mathbf{r}_{34})\otimes\mathbf{r}_{14}](\mathbf{r}_{12}\cdot\mathbf{r}_{23})(\mathbf{r}_{23}\cdot\mathbf{r}_{34})}{(r_{12}r_{23}r_{34})^n r_{14}^m},$$

where $\boldsymbol{r_{ij}} = \boldsymbol{r_i} - \boldsymbol{r_j}$ and $\hat{\boldsymbol{r}}_{\boldsymbol{ij}} = \boldsymbol{r_{ij}}/r_{ij}$ and n and m are arbitrary integers and ρ stands for the density of concentration. A scaled chiral index G_{0S} is a summation of contributions of all sets of four atoms in a numerical evaluation given by

$$G_{0S}=\frac{4!}{N^4}\frac{1}{3}\left[\sum_{\substack{\text{all permutations of}\\ i,j,k,l=1\cdots N}} w_i w_j w_k w_l \times \frac{[(\mathbf{r}_{ij}\times\mathbf{r}_{kl})\cdot\mathbf{r}_{il}](\mathbf{r}_{ij}\cdot\mathbf{r}_{jk})(\mathbf{r}_{jk}\cdot\mathbf{r}_{kl})}{(r_{ij}r_{jk}r_{kl})^n r_{il}^m}\right], \qquad G_{0S}=\frac{4!}{N^4}G_0,$$

where N is total number of atoms in molecule, w is atomic weight =1 for all molecules considered here to provide a measure of steric chirality [4]. In our calculation, we have obtained the scaled chiral index by calculating summation of contributions of all sets of four points from nine coordinates (primary and secondary center of masses, Table S1) using in-house MATLAB codes for OPD [2,5] and UCSF Chimera[6].

Single particle scattering measurements

Transmission dark field scattering spectra are collected by a microspectrophotometer (CRAIC 308 PV) integrated on an optical microscope (Olympus BX51). White light from a 100 W tungsten halogen lamp is focused onto the sample drop casted on a glass substrate by using a substage dark field condenser (Olympus U-DCD), and dark field scattering from the sample is collected by a 40x objective (Olympus Plan N, NA 0.65). At 40x magnification, the collection aperture of the microspectrophotometer corresponds to a sample region of 6.9 μm × 6.9 μm. The measured scattering intensity spectra is normalized by the lamp spectrum measured from a diffuse scattering reference (Labsphere) and using the expression $I_{scat} = (I_{sample} - I_{sample,\ background})/(I_{ref} - I_{ref,\ background})$. See **SI figure 42** for the corresponding data.

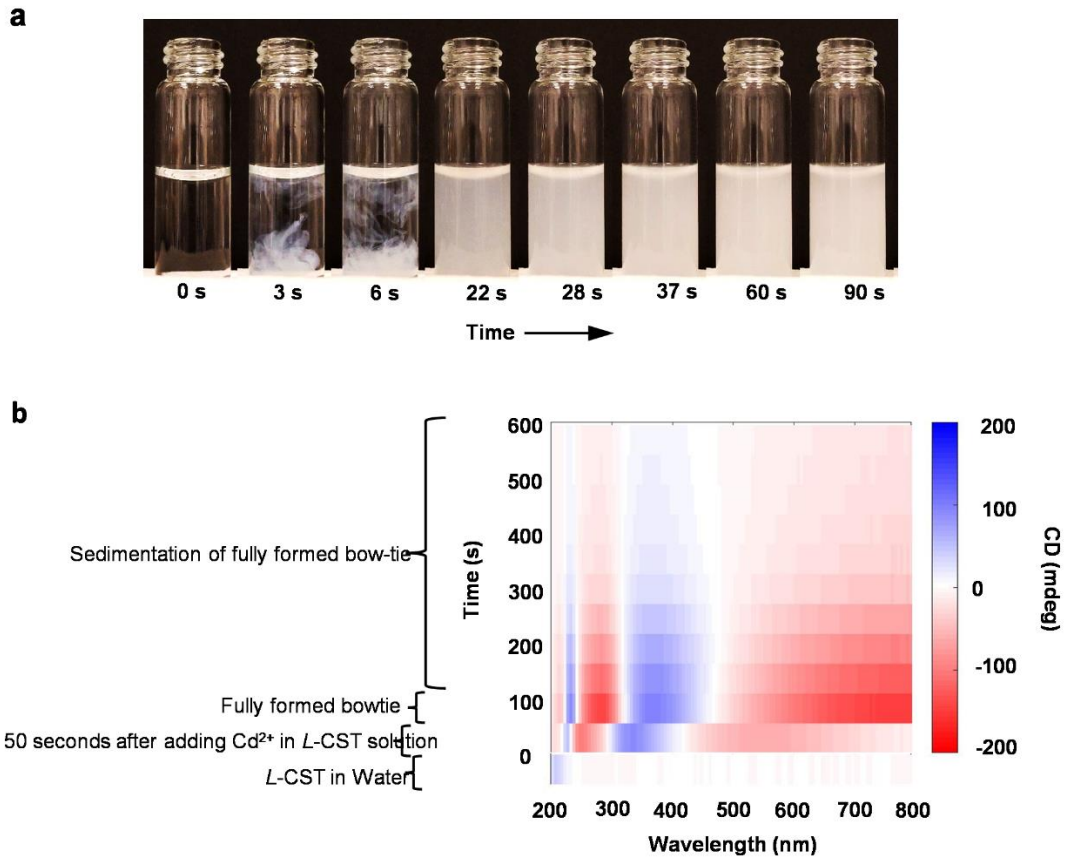

SI Fig 1. Self-assembly of bowtie particles. a, Photographs of the change in turbidity of the [*L*-CST] = 1 mM solution upon addition of [Cd^{2+}] = 1 mM ions as time increases. The rate of change in turbidity is proportional to the [Cd^{2+}] where higher concentration of metal ion causes a faster change in turbidity. **b,** CD spectra of bowtie particle dispersions acquired during their formation.

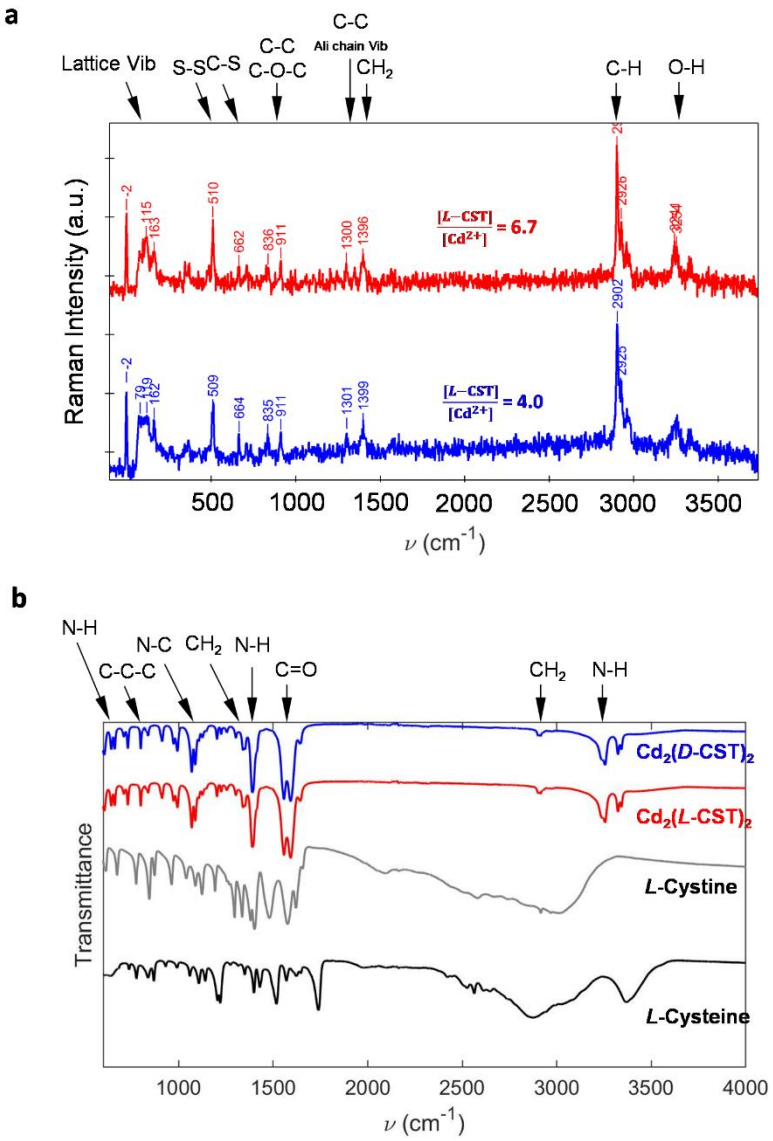

SI Fig 2. Vibrational spectroscopy of the bowtie particles. a, Raman spectra from two different bowtie morphologies assembled with different starting [*L*-CST] and [Cd^{2+}]. Both synthetic conditions result in different macroscale morphology but same Raman spectra indicating that the molecular structure of smallest building blocks are same. **b,** FTIR spectra of *L*-cysteine (free amino acid, not cystine), *L*-CST, bowties from *L*-CST and *D*-CST in powder form.

Note: Presence of S-S disulfide stretches in Raman spectra around 500 cm^{-1} is a confirmation that dipeptide bond is not broken in the self-assembled structure. As compared to *L*-CST bowties have a weak broad shoulder peak in 3000-3750 cm^{-1} range with sharp peaks on top of it, indicating the presence of directional hydrogen bonding.

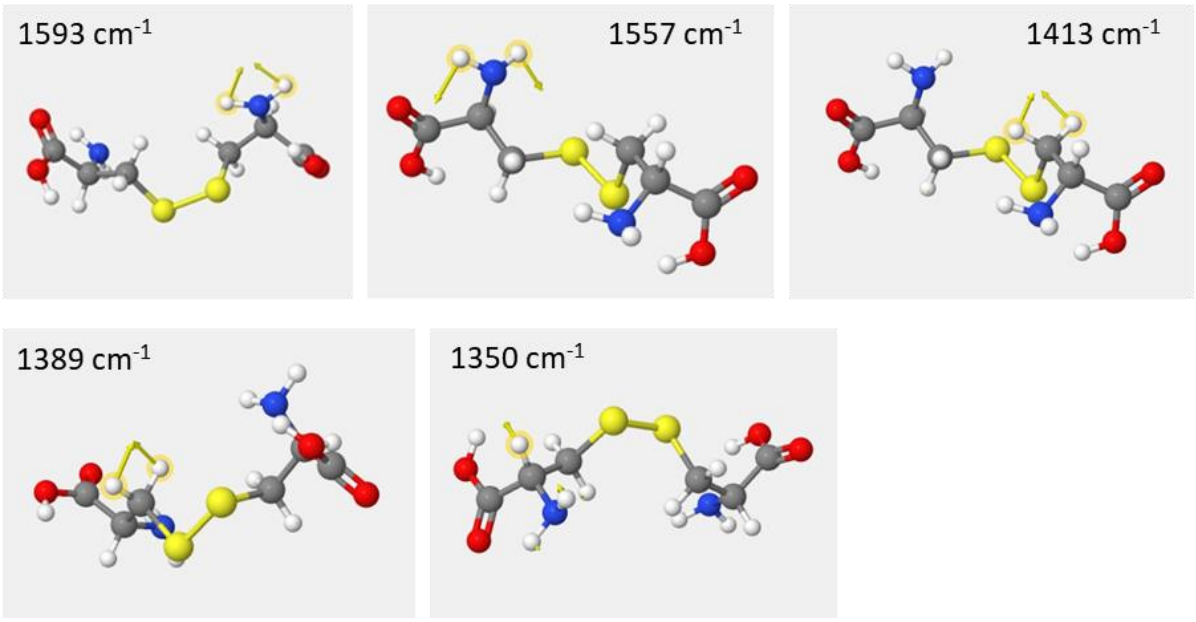

SI Fig 3. Simulated vibrational configurations of a Cystine molecule at which the Cd_2CST_2 bowties demonstrate chiral fingerprint in VCD spectrum. Note the -NH_2 scissoring inwards (1593 cm^{-1}) and outwards (1557 cm^{-1}) are the most intense in the VCD spectra.

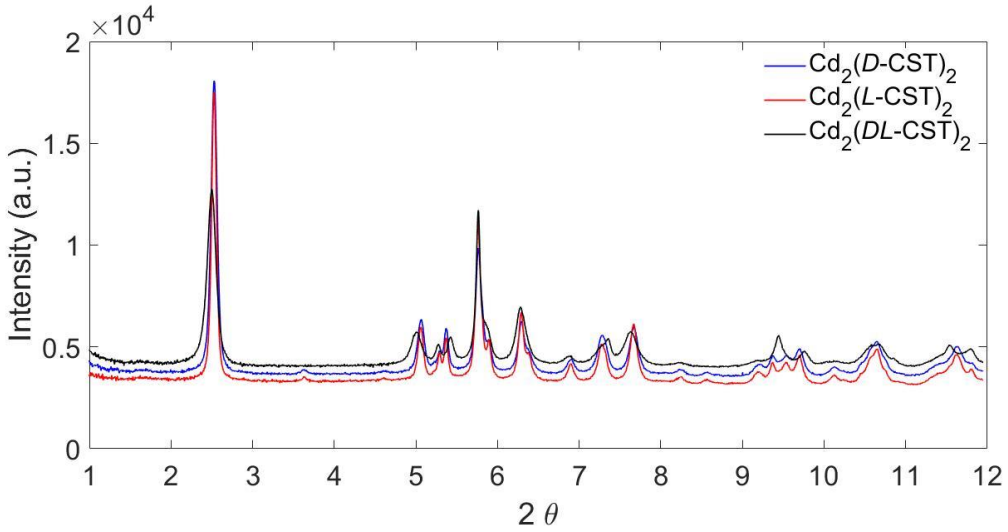

SI fig 4. Synchrotron XRD data for freeze-dried powders of Cd_2(*L*-CST)$_2$ (red), Cd_2(*D*-CST)$_2$ (blue) and Cd_2(*DL*-CST)$_2$ (black) bowties are plotted.

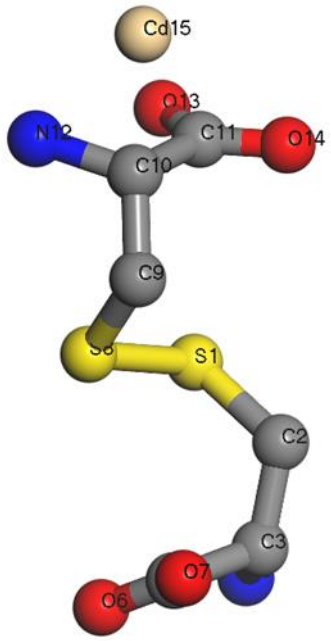

SI Fig. 5. Atomic structure of the atomic unit in the constituent nanocluster, comprising of *L*-CST molecule, Cd^{2+} used for the simulated annealing procedure in structure solution.

Table 1. Experimental details

Crystal data	
Chemical formula	$C_6CdN_2O_4S_2$
M_r	340.62
Crystal system, space group	Orthorhombic, $P2_12_12_1$
Temperature (K)	298
a, *b*, *c* (Å)	20.454 (2), 9.9230 (9), 5.0438 (4)
V (Å^3)	1023.68 (17)
Z	4
Radiation type	Synchrotron mono-beam
Data collection	
Diffractometer	Debye-scherrer geometry diffractometer with area detector at Beamline 17-BM
2θ values (°)	$2\theta_{min}$ = 0.80 $2\theta_{max}$ = 16.82 $2\theta_{step}$ = 0.01
Refinement	
R factors and goodness of fit	R_p = 0.021, R_{wp} = 0.027, $R(F^2)$ = 0.1333, χ^2 = 5.272

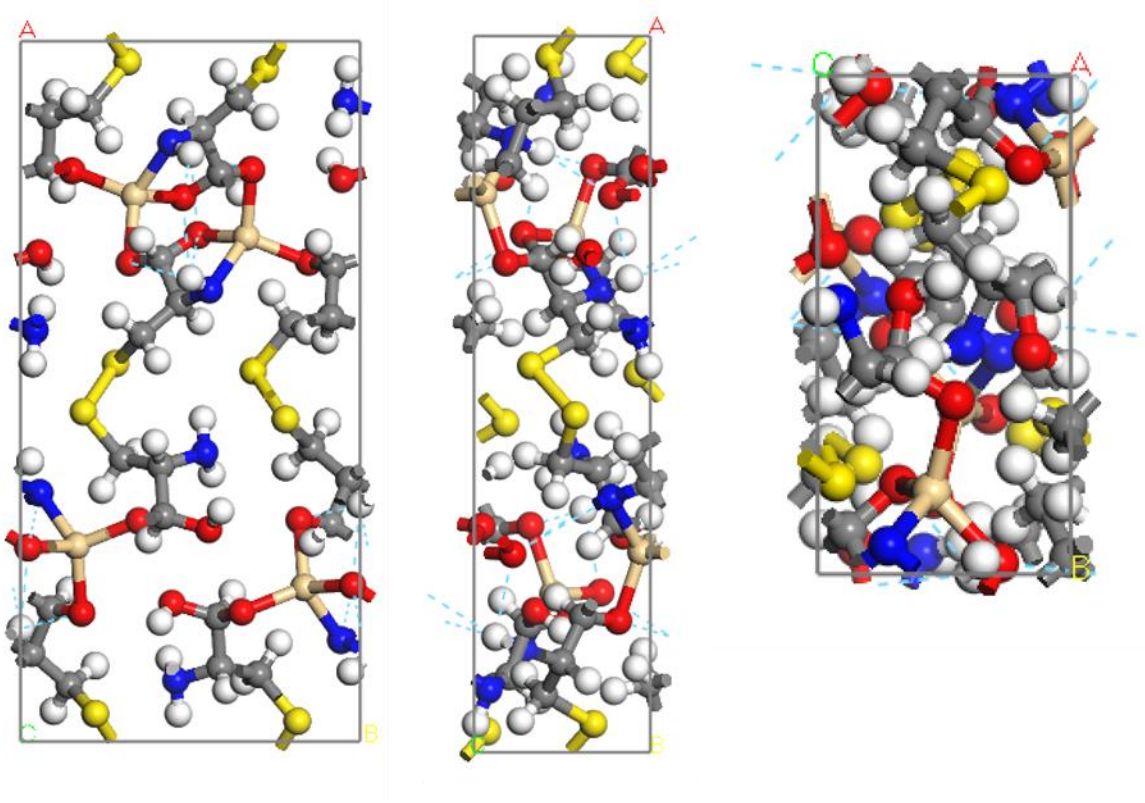

SI Fig 6. Three perpendicular projections of the atomic structure of the refined structure of Cd_2(*L*-CST)$_2$ unit cell. Atoms are represented as Oxygen (red), Carbon (black), Cadmium (Brown), Nitrogen (blue), Sulfur (yellow).

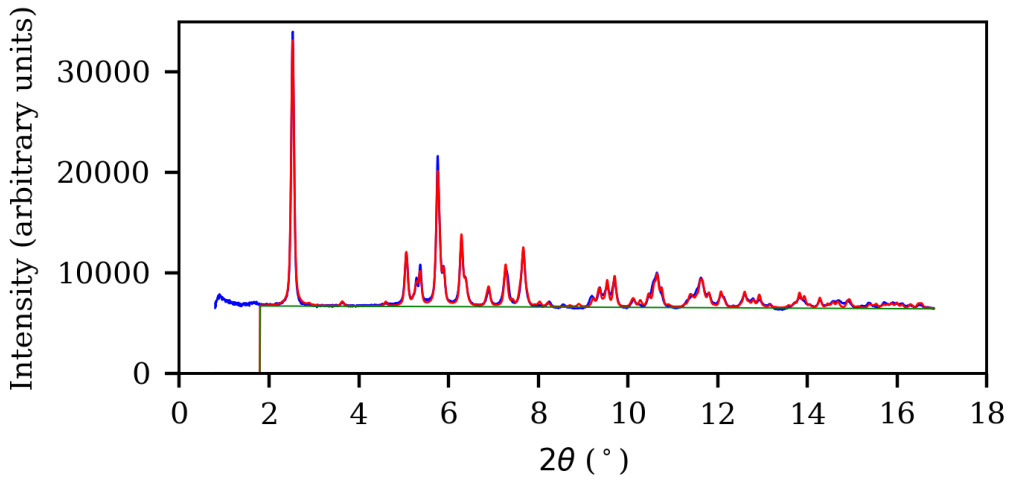

SI Fig 7. Comparison between the observed (blue) and calculated XRD spectra (red) obtained from the solved structure.

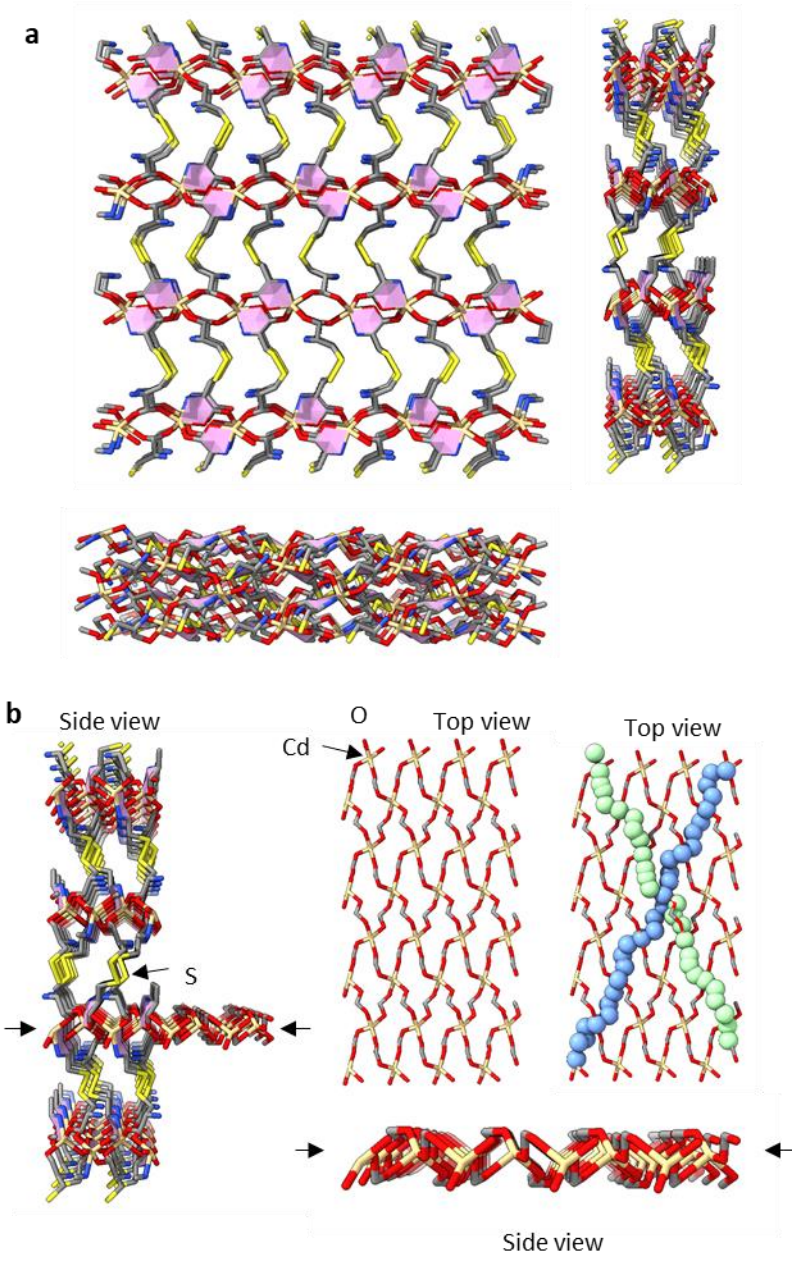

SI Fig 8. a, Atomic structure of 4x2x2 Cd_2(L-CST)$_2$ supercell of bow-ties is shown along [001], [010], and [100] zone axis. **b,** Side view of the supercell with the layer of Cd-O is extended out for clarity. The top view of the Cd-O layer is shown on the right with the helical chains are highlighted with spherical markers.

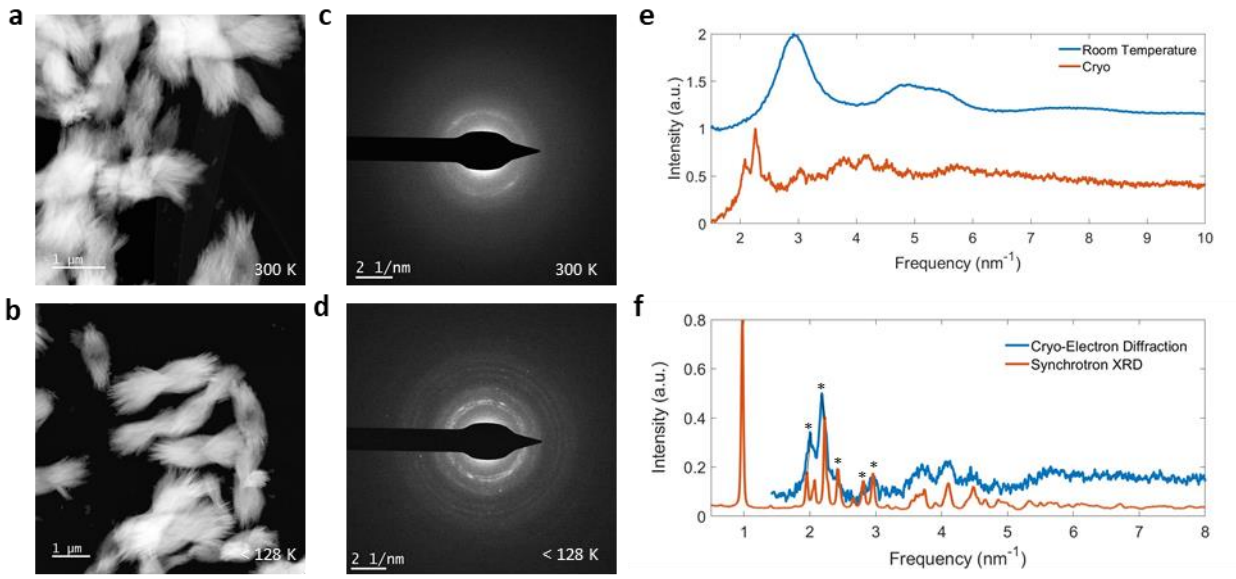

SI Fig 9. Electron dose sensitivity of bowties. a,b, Annular dark field scanning transmission electron microscopy (ADF-STEM) image and **c,d,** corresponding electron diffraction pattern (right) for bowties at room temperature (300 K) and cryogenic temperature (below 128 K). At room temperature the Cd-CST bowties convert into CdS chiral particles as evidenced by emergence of the broad peaks at 2.9 nm^{-1} and 4.8 nm^{-1} characteristic of CdS. **e,** Line spectra of the rotationally averaged electron diffraction pattern shown in panels **c** and **d** at 300 K (blue) and < 128 K (orange). **f,** Electron diffraction pattern obtained at <128 K (blue) and synchrotron XRD pattern (orange) confirming the transition of bowties into nanoparticles under the electron beam at room temperature. The primary peak in XRD pattern corresponding to inter-chain distance at 10.2 Å is blocked by the beam stopper in SAED pattern.

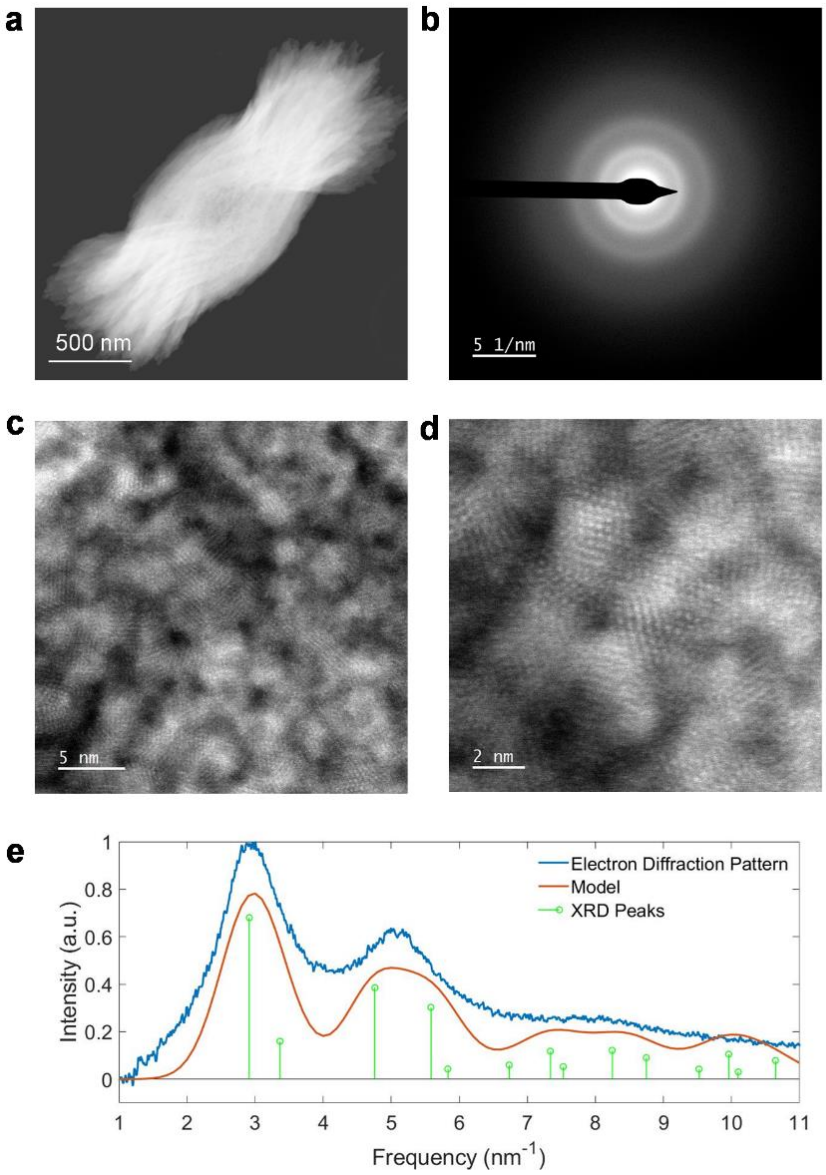

SI Fig 10. Conversion of Cd-CST bowties into CdS bowties. a, ADF-STEM image and **b,** Electron diffraction pattern of bowties. **c,d,** High-resolution ADF-STEM image of bowtie shown in a, confirming the presence of 2-5 nm sized NPs of CdS. **e,** Rotationally averaged electron diffraction (blue) shown in panel b, with a modeled electron diffraction for 2.5 nm sized NPs (orange). The corresponding peaks of CdS from crystallographic database for PDF 10-0454.

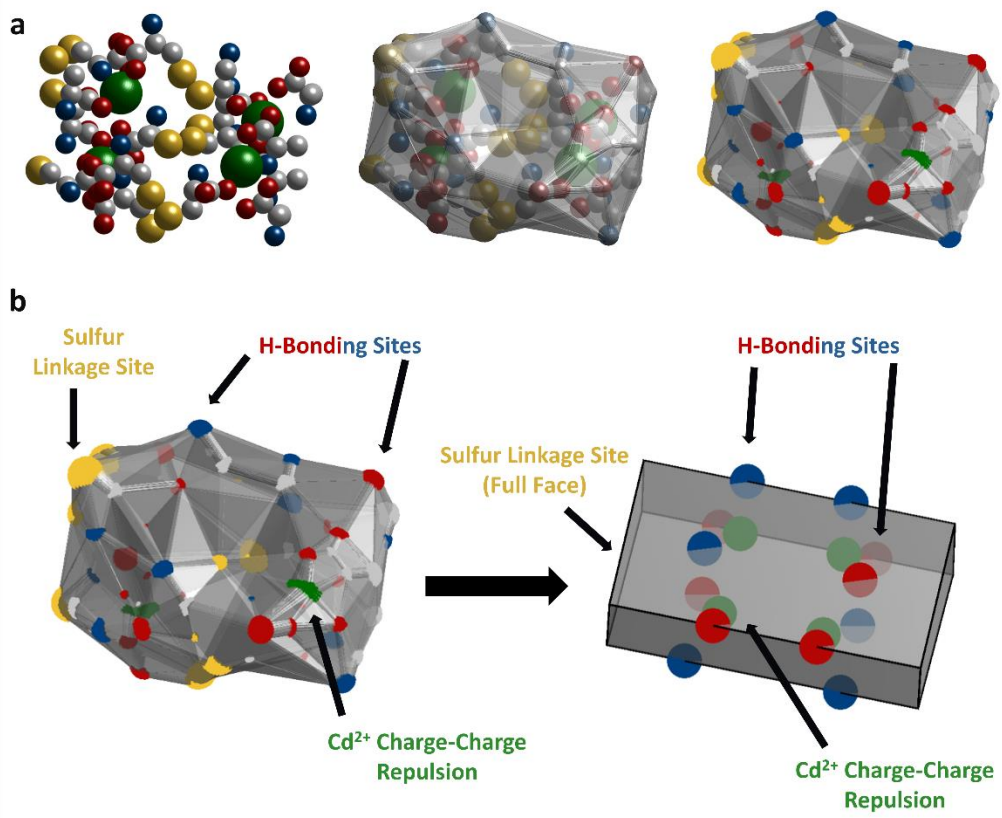

SI Figure 11. Coarse-grained model of the Cd-CST nanoclusters. a) (Left) XRD resolved structure of building block. (Middle) Convex hull around atoms. (Right) Patchy model of convex hull of the nanocluster. b) Construction of generalized building block. Relevant features such as sites for hydrogen bonding (H-bonding), charge-charge repulsion, and sulfur linkage sites are placed on the generalized building block to mimic their general location on the XRD resolved patchy convex hull of the nanocluster in **a**).

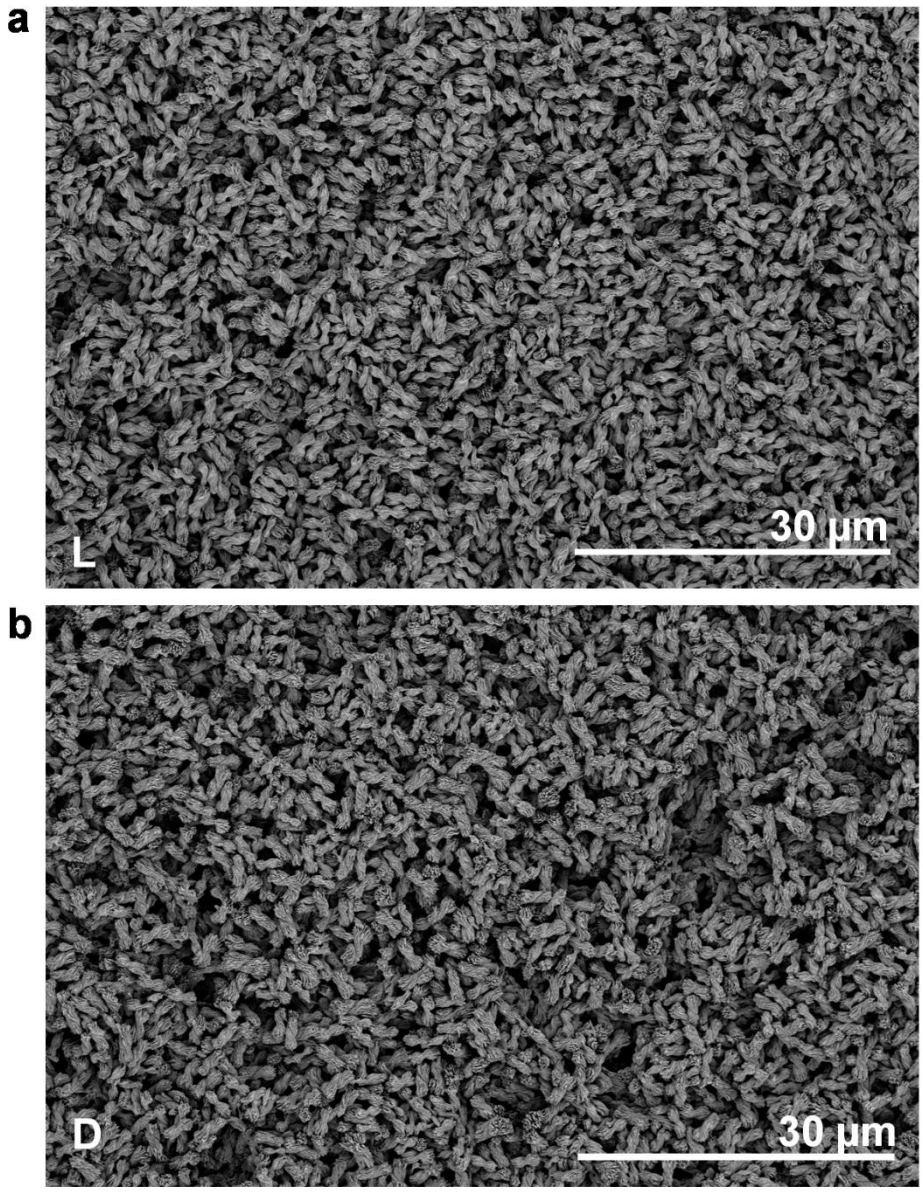

SI Fig 12. Monodispersity of the self-assembled bowties. SEM images of the **a,** Cd_2(*L*-CST)$_2$ and **b,** Cd_2(*D*-CST)$_2$ bowties formed from [*L*-CST] and [Cd^{2+}] as 4 mM in 200 ml water.

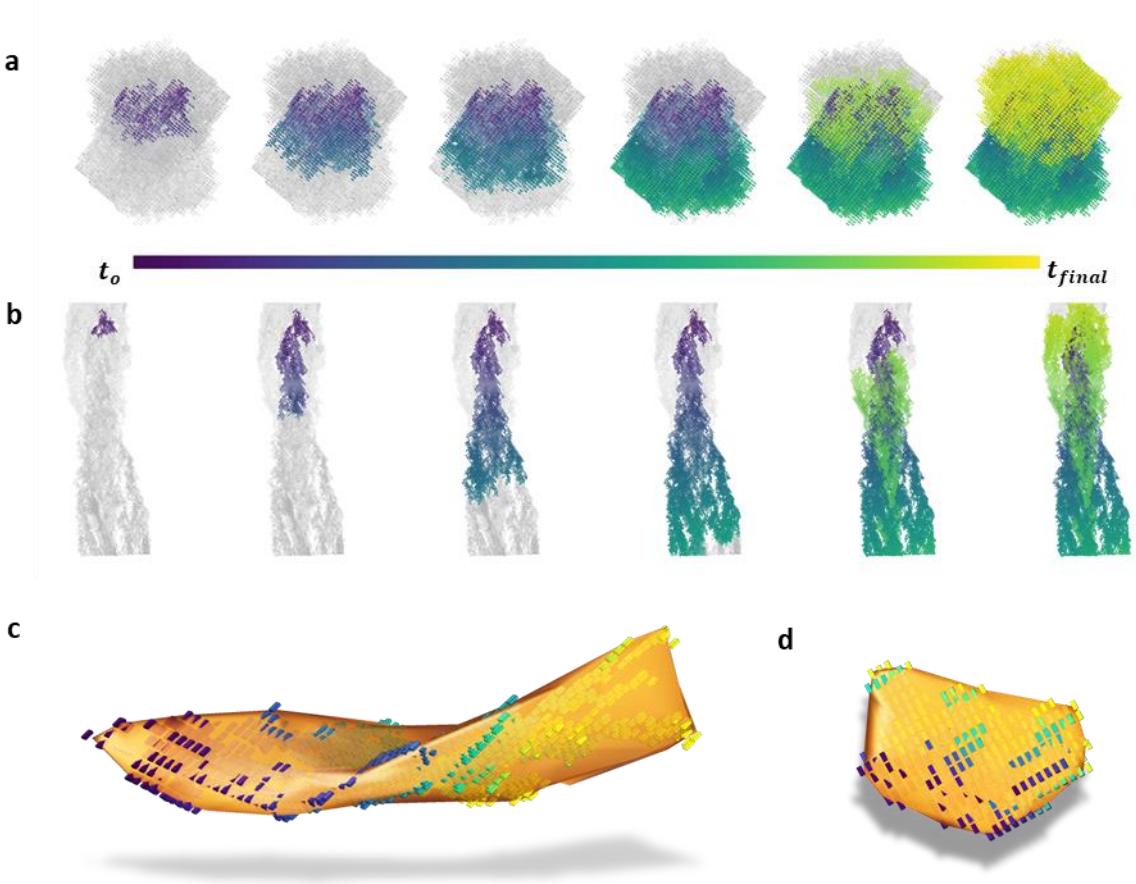

SI Fig 13. Monte-Carlo simulation of the growth of nanoribbons and their stacks. Snapshots of particle growth simulations for **a,** $\chi = 0$ and **b,** $\chi = 1$. Ordered domains are visible in both growth conditions. Smallest ordered domains during initial stages of growth are shown for **c,** $\chi = 1$ and **d,** $\chi = 0$. Colors of the individual units represent the normalized time at which the nanoribbons attach to the existing bowtie particle.

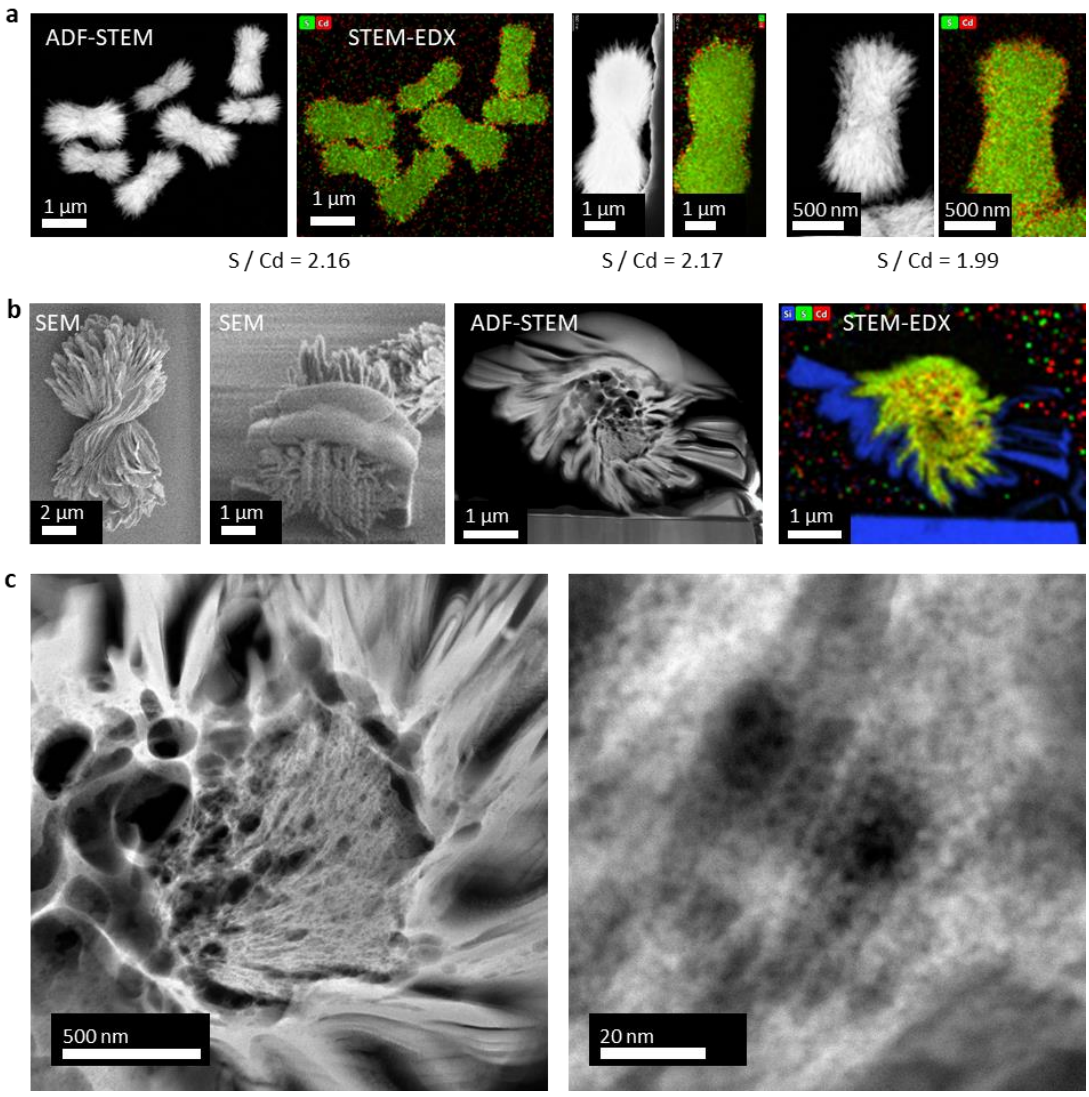

SI Fig 14. STEM-EDX based evaluation of atomic distribution. a, Spatially resolved energy dispersive X-ray spectroscopy for the bowties made with different [Cd^{2+}], [*L*-CST] concentrations. Atomic concentration of S (green) and Cd (Red) was in the ratio 2:1, indicative of one CST molecule sharing one Cd atom. This ratio was used to construct a Cd-CST fragment as an input for atomic structure solution from 3D electron density maps obtained from powder XRD data. The presences of extra Cd^{2+} at the interface indicates positive surface charge. **b,** Cross-sectional analysis of the bowtie at the center node was performed and revealed the S/Cd ratio of 1.67, which could occur due to transformation by Ga-ion beam during thinning or due to a difference in the core composition. **c,** High-resolution ADF-STEM images of the core of a right-handed bowtie indicate a fibrous structure made of polydisperse NPs.

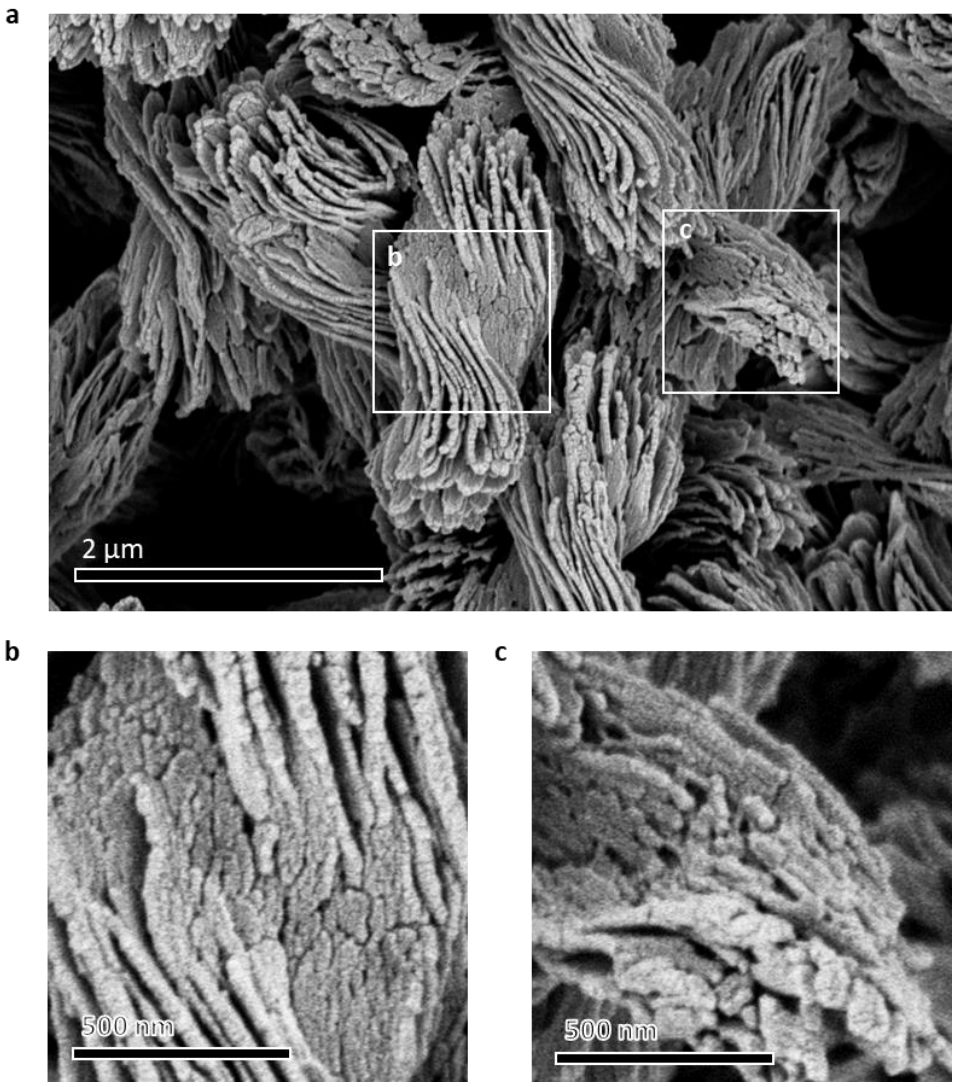

SI Fig 15. High magnification SEM images of bowtie particles. Shown here are the SEM images of **a,** fully formed bowtie, **b,** magnified region at the center of bowtie and **c,** magnified region at the edges of the bowtie. Synthesis conditions are $[Cd^{2+}]$ = 4 mM, [*L*-CST] = 4 mM, Water = 200 ml. Polydisperse nanoplatelets with diameters between 20-100 nm are assembled into nanoribbons. In turn, they are stacked into the bowties with the left twist. Smaller nanoplatelets lead to stronger twisting.

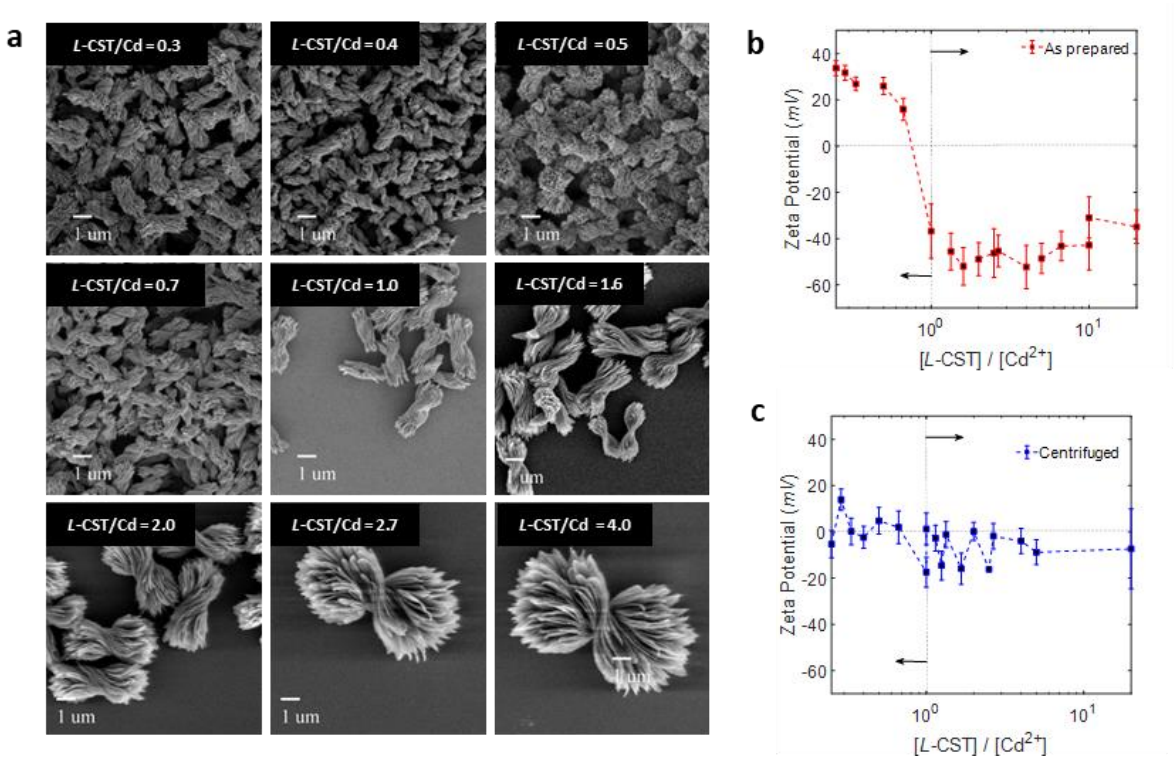

SI Fig 16. Geometry of the bowtie particles made with different *L*-CST/Cd ratios. Geometrical parameters characterizing length, width and thickness of the bowties, namely *l*, *w*, and *t* depicted in **Fig. 3c**, increase with the increase of [*L*-CST]/[Cd^{2+}] ratio. **b,** Zeta potentials (red) of as-made bowtie particles made with different [*L*-CST]/[Cd^{2+}] ratios in the original synthetic media increases with crossover at 0 potential occurring near [*L*-CST]/[Cd^{2+}] = 1. **c,** Zeta potentials of bowtie particles made with different [*L*-CST]/[Cd^{2+}] ratios after centrifugation and re-dispersion in DI water. Comparison with the zeta-potentials in original reaction media indicate that the charge of the bowtie surface is associate with adsorption of excess ions of *L*-CST or Cd^{2+} depending on the [*L*-CST]/[Cd^{2+}] ratios. The excess positive and negative charge is depleted upon centrifugation.

Note: The dependence *l*, *w*, and *t* of the fully assembled particles is consistent with the dependence of thickness and width of individual nanoribbons on [*L*-CST] and *L*-CST/Cd ratio (see also **Fig. SI 20,26**).

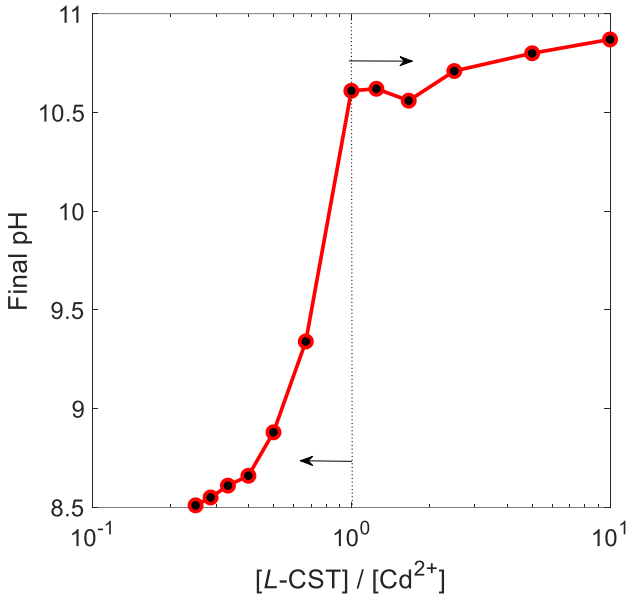

SI fig 17. Change in pH of the solution as the ratio of [*L*-CST]/[Cd^{2+}] is changed.

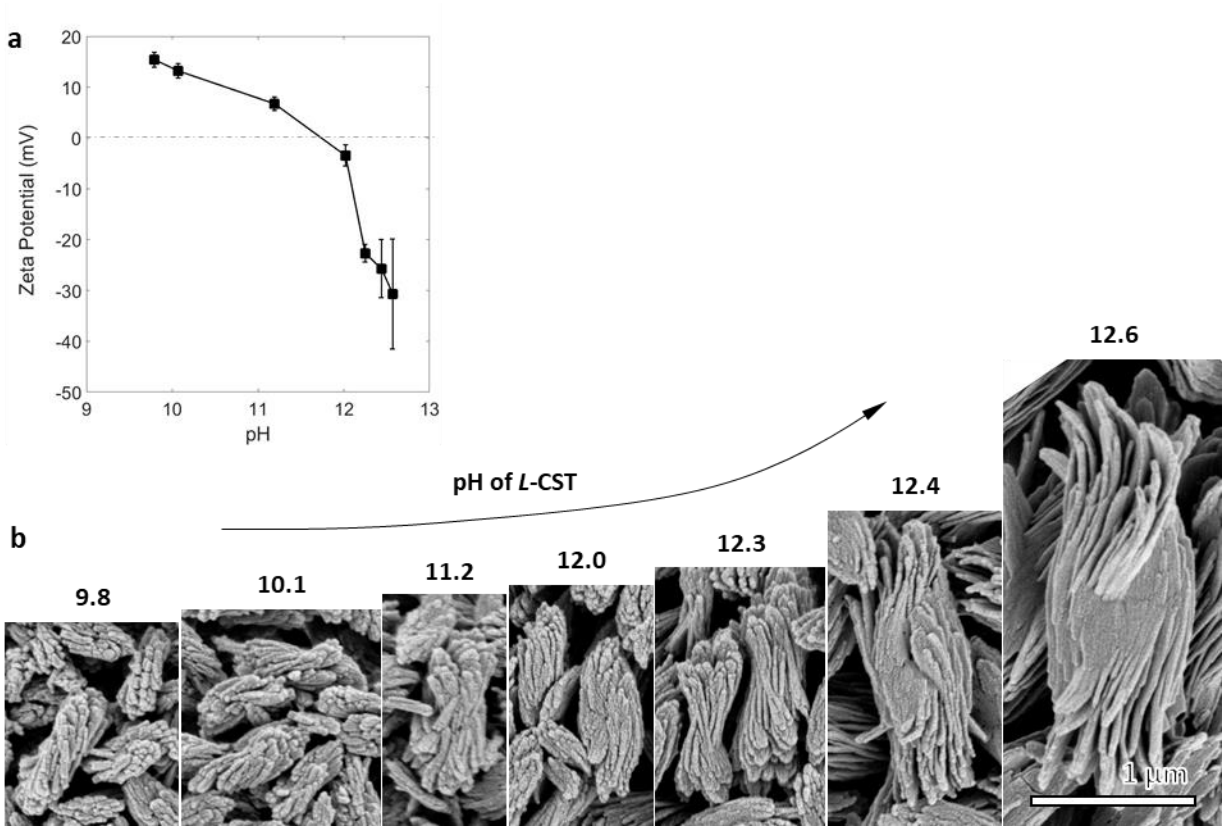

SI Fig. 18. Role of pH in self-assembly. a, Variation of zeta-potential of fully formed particles with increasing pH of [*L*-CST] = 4 mM solution before addition of [Cd^{2+}] = 4 mM. pH was controlled by adding NaOH in the range of 0.7 to 1 ml volume to a 10 ml solution of *L*-CST. Cystine is typically soluble above pH 8 and below pH 2. **b,** SEM images of the self-assembled bowties after addition of Cd^{2+} ions to the corresponding *L*-CST solution. It is notable that the twisting of the self-assembly begins above pH 12, which also coincides with the negative zeta potential of the bowties. Scale bar across all images in 1 um.

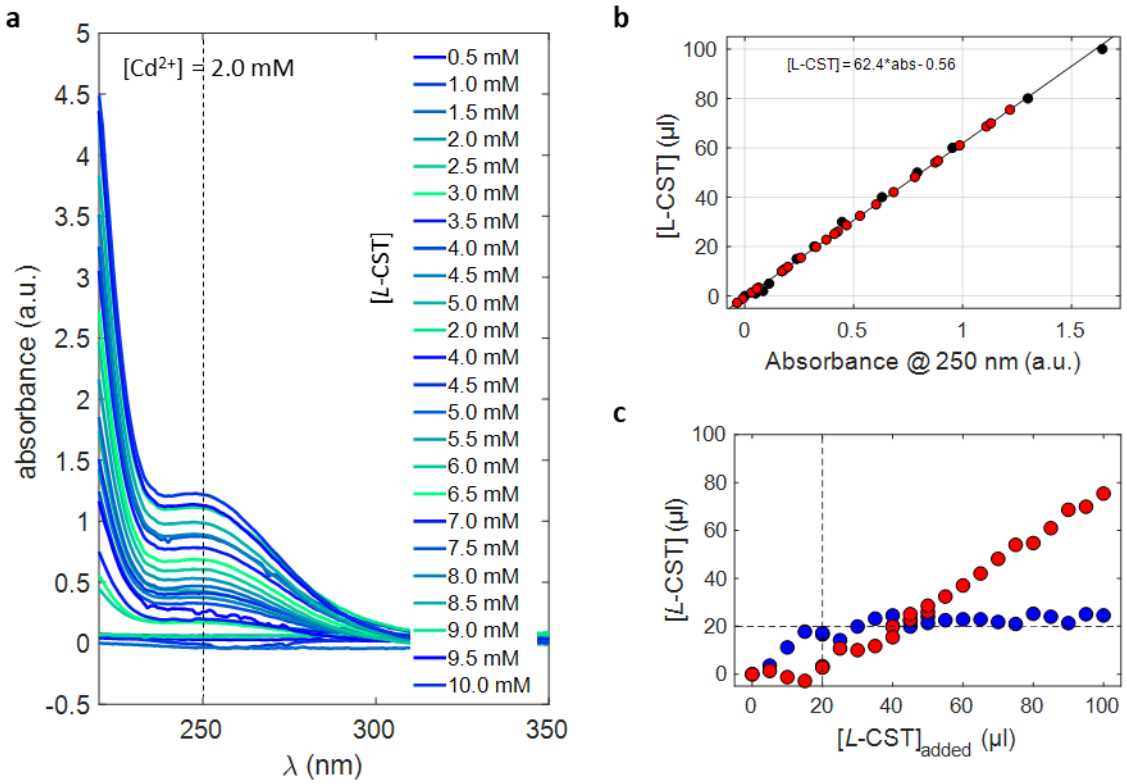

SI Fig 19. Quantification of the consumed *L*-CST during the bowtie synthesis. a, Absorbance of supernatant from reactions of [Cd^{2+}] = 2 mM with varying [*L*-CST] (0.5 mM to 10 mM). **b,** Calibration chart for absorbance of [*L*-CST] vs absorbance at 250 nm is shown here with black circles representing absorbance from only [*L*-CST] and red-circles representing estimating [*L*-CST] in supernatant. **c,** [*L*-CST] vs [*L*-CST] added for samples shown in panel a. Up to 20 µl or (2mM) [*L*-CST], all added [*L*-CST] is consumed (blue curve) and the curve is linear. Beyond 20 µl added [*L*-CST], 21.7 ± 2.9 µl is consumed, indicating that the [Cd^{2+}] and [*L*-CST] interact in 1:1 ratio to precipitate the bowties.

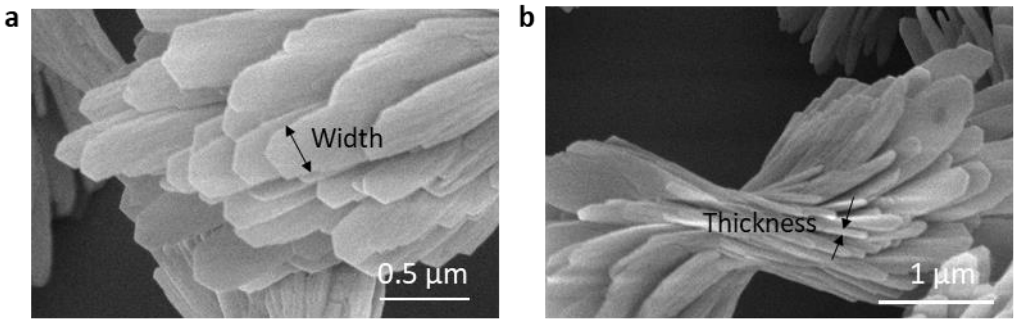

c

[*L*-CST]	[Cd^{2+}]	[*L*-CST]/[Cd^{2+}]	Width	Thickness
50 ul	20 ul	2.5	470 ± 70 nm	70 ± 10 nm
40 ul	20 ul	2.0	500 ± 60 nm	90 ± 20 nm
30 ul	20 ul	1.5	320 ± 20 nm	50 ± 10 nm
20 ul	20 ul	1.0	130 ± 30 nm	45 ± 5 nm
10 ul	20 ul	0.5	50 ± 8 nm	30 ± 7 nm

SI Fig 20. Geometry of the nanoribbons for various synthetic conditions. SEM image of the ribbons **a,** facing the electron beam and **b,** resting on the silicon wafer in edge-on orientation. c, Tabulated width and thickness for changing [*L*-CST] / [Cd^{2+}] ratio. As [*L*-CST] and [*L*-CST] / [Cd^{2+}] ratio decreases, the width and thickness of the nanoribbons also decrease.

Note: The correlation with [*L*-CST] and [*L*-CST]/[Cd] ratio is fully consistent with that of the length, width and thickness of the entire assembled particles (SI **Fig.** 26). Increasing the concentration of ions in the system for CST and Cd^{2+} is not the same. If we increase the CST we are increasing the number of –COO and $–NH_2$ groups which simply extend the long range order over several length scales. However, increasing the Cd^{2+} ion concentration changes the platelet charge to positive because they get adsorbed on the negatively charged surface. This creates a repulsion between positively charged platelets but they cannot form hydrogen bonds over long range, because carbonyl groups are limited and therefore the overall size of the bowtie decreases. In the figure above as [*L*-CST]/[Cd^{2+}] ratio increases that means relative concentration of [Cd^{2+}] ions are decreasing in number, so the sheets should be negatively charged.

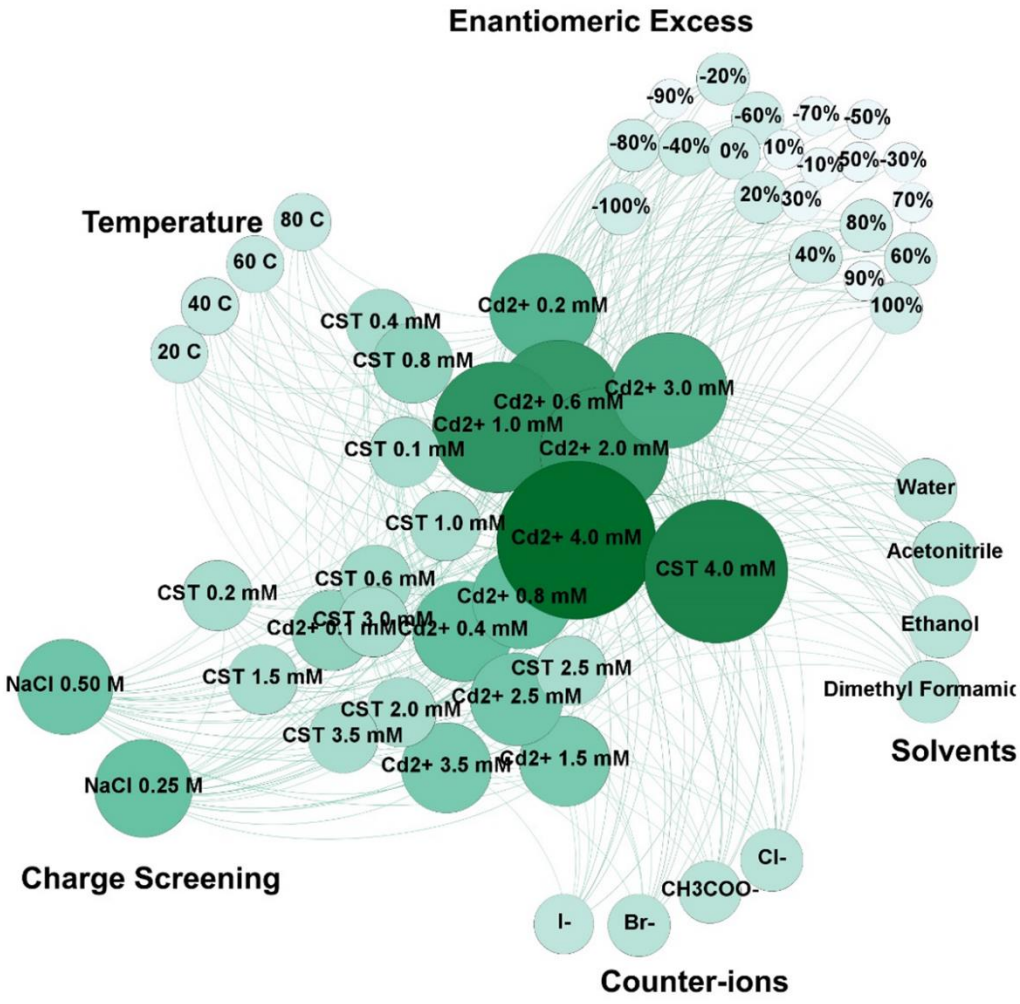

SI Fig 21. Schematic of the different physicochemical parameters used to exert structural control over the bowtie assemblies. Changing one or two parameters (such as temperature, EE, counter-ions, solvents, and NaCl) with varying [Cd^{2+}] and [*L*-CST] results in a wide range of continuously variable bowtie assemblies.

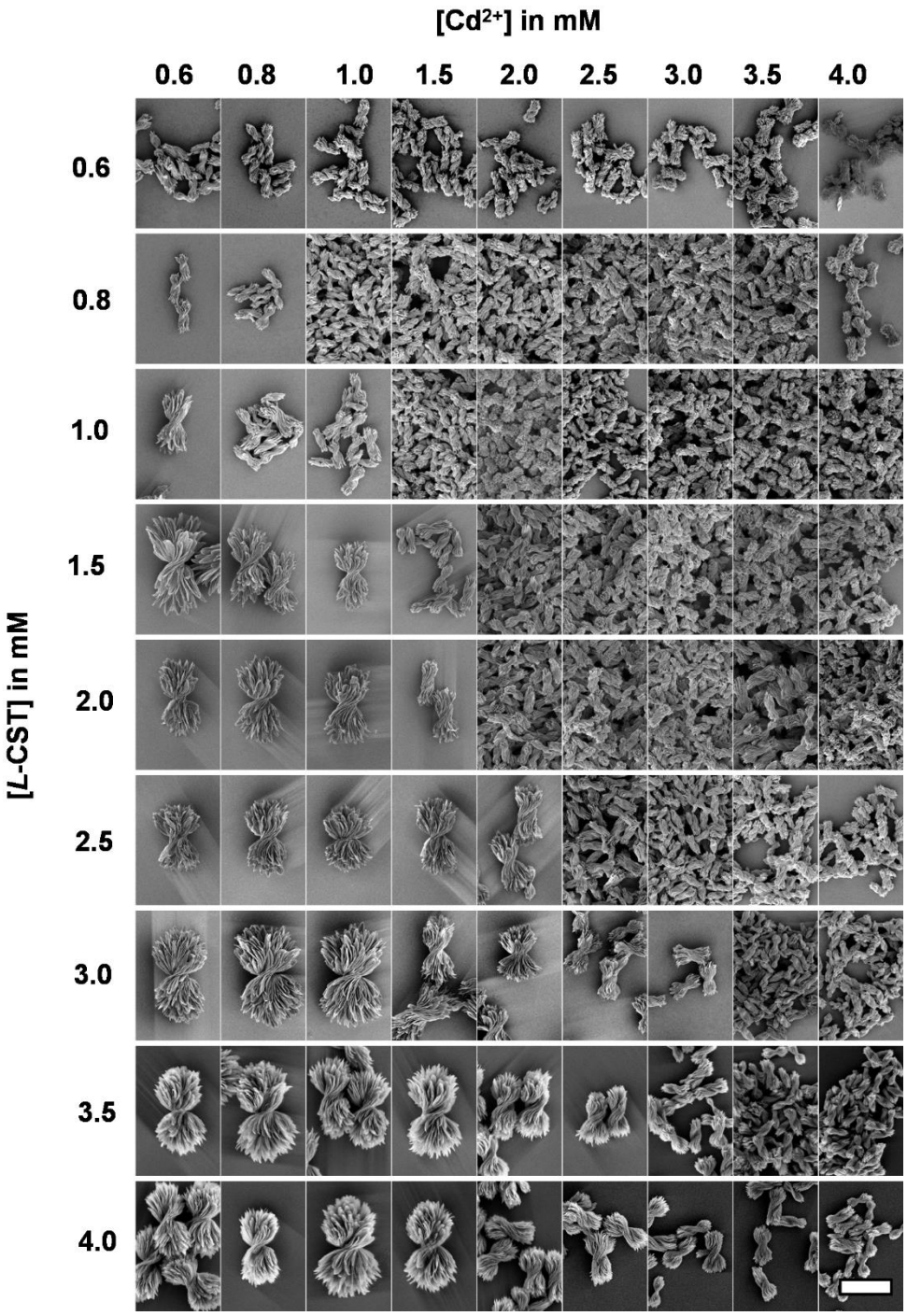

SI Fig 22. Phase diagram for the combinations of [*L*-CST] and [Cd^{2+}] concentrations varying from 0.6 mM to 4 mM. Increase in [*L*-CST] with [Cd^{2+}] constant (along the columns) results in increase in size of bowties. Increase in [Cd^{2+}] while keeping [*L*-CST] constant (along the rows) results in decrease in size of bowties. Scale bar is 5 μm.

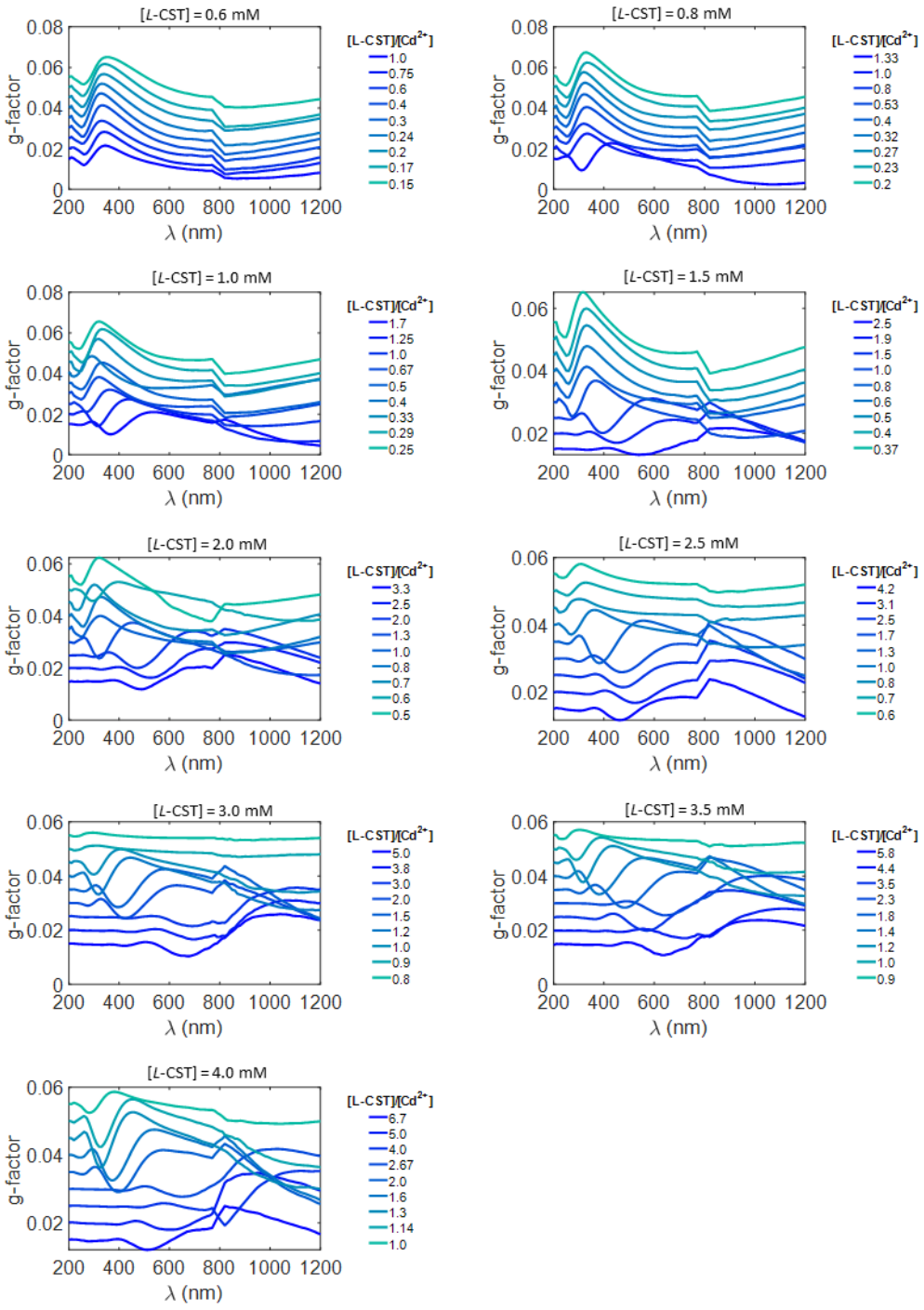

SI Fig 23. g-factor spectra from UV-vis to NIR region is plotted for fixed [*L*-CST] concentration corresponding to each row in phase diagram shown in SI Fig 22. As the [*L*-CST] concentration increases, the variations in g-factor spectra are amplified. From 800-1200 nm the detector changes resulting in a jump in the spectra due to gain correction differences between two detectors.

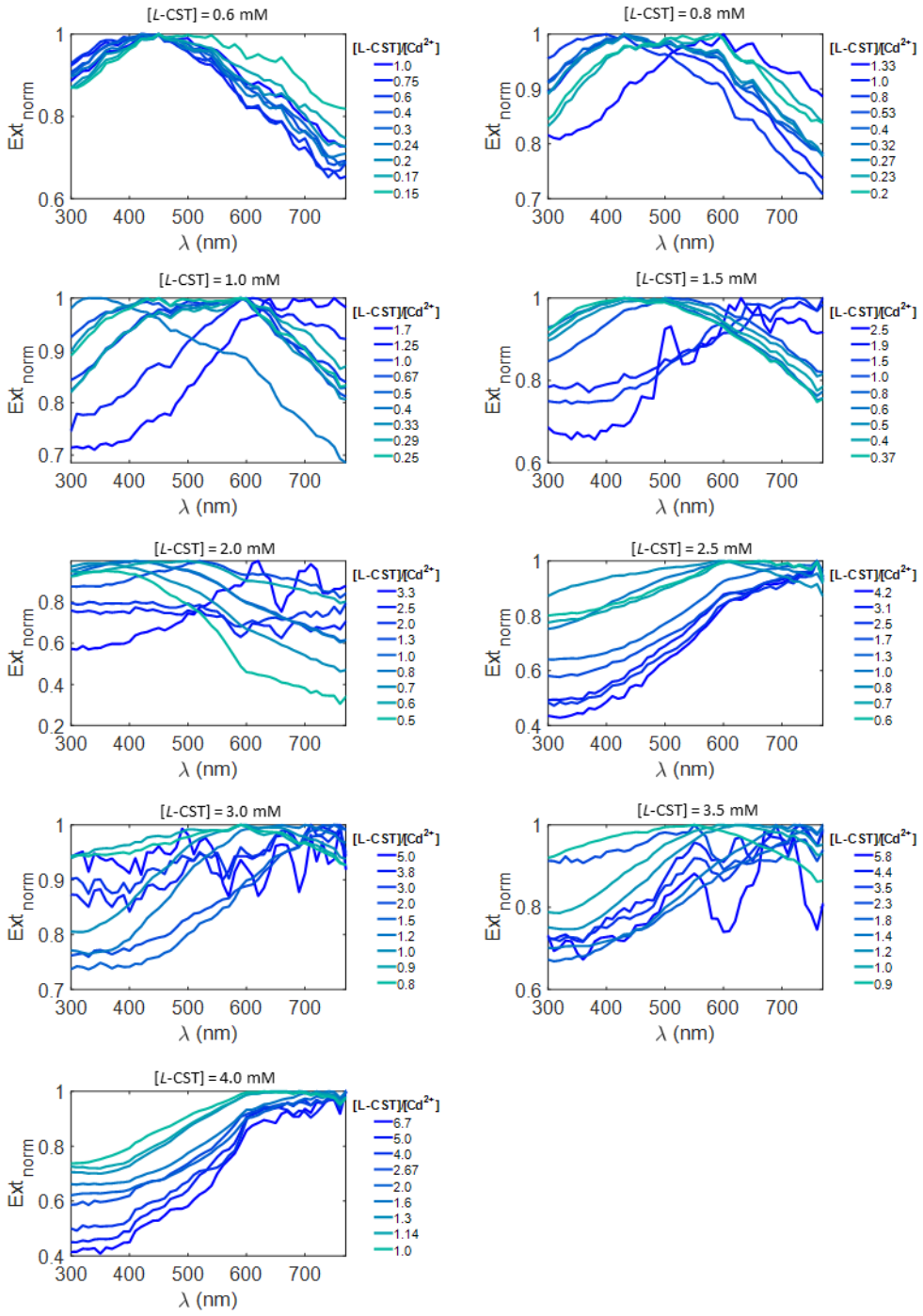

SI Fig 24. Normalized extinction spectra is plotted for fixed [*L*-CST] concentration corresponding to each row in phase diagram shown in SI Fig 22. As the [*L*-CST] concentration increases, the extinction peak red-shifts. Some extinction spectra have a lower signal to noise ratio because of lower particle concentration of larger sample in 1ml vial.

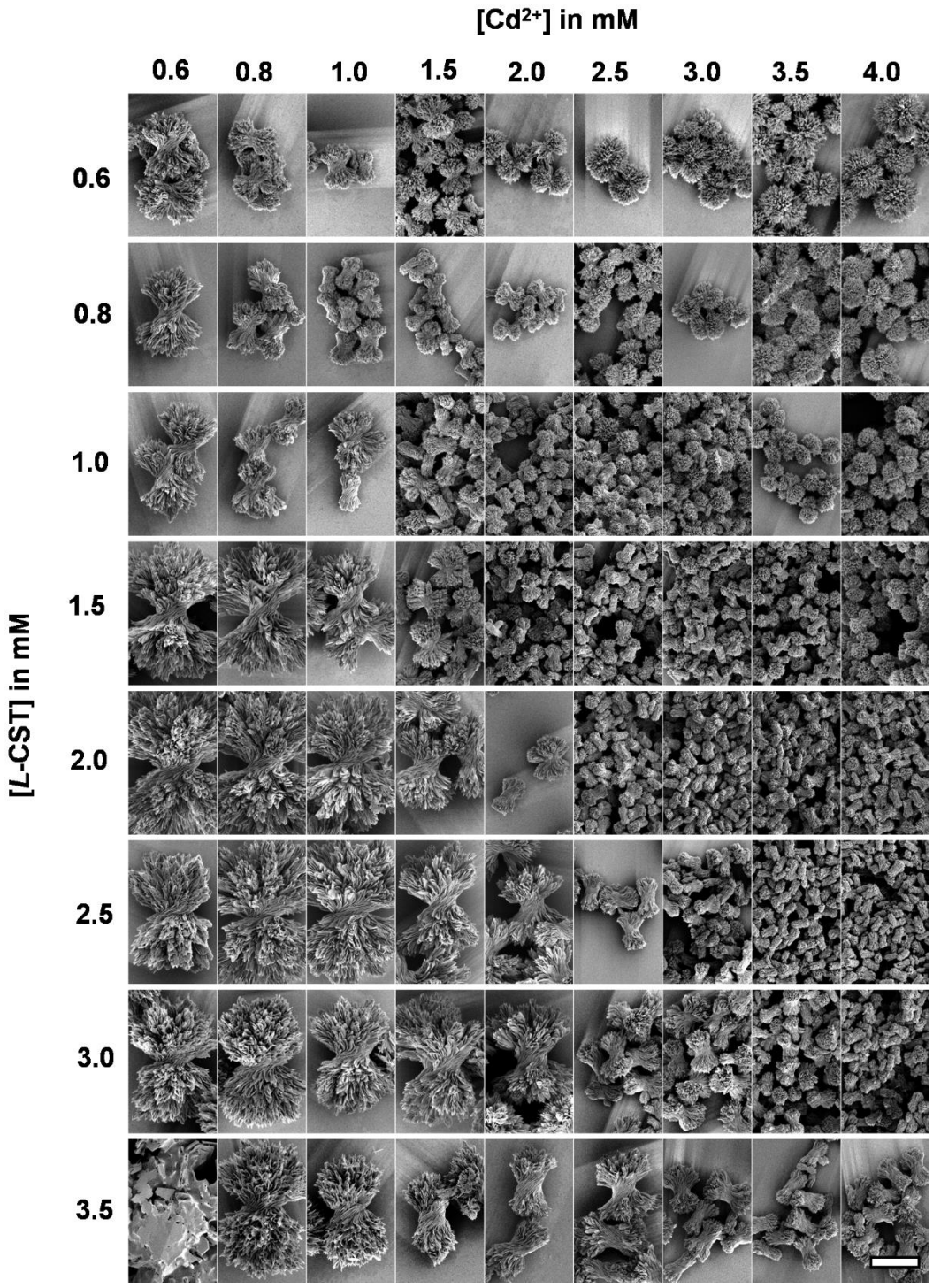

SI Fig 25. Phase diagram for the combinations of [*L*-CST] and [Cd^{2+}] concentrations varying from 0.6 mM to 4 mM in the presence of added 0.25 M NaCl in water. Increase in [*L*-CST] with [Cd^{2+}] constant (along the columns) results in increase in size of bowties. Increase in [Cd^{2+}] while keeping [*L*-CST] constant (along the rows) results in decrease in size of bowties. Scale bar is 5 μm.

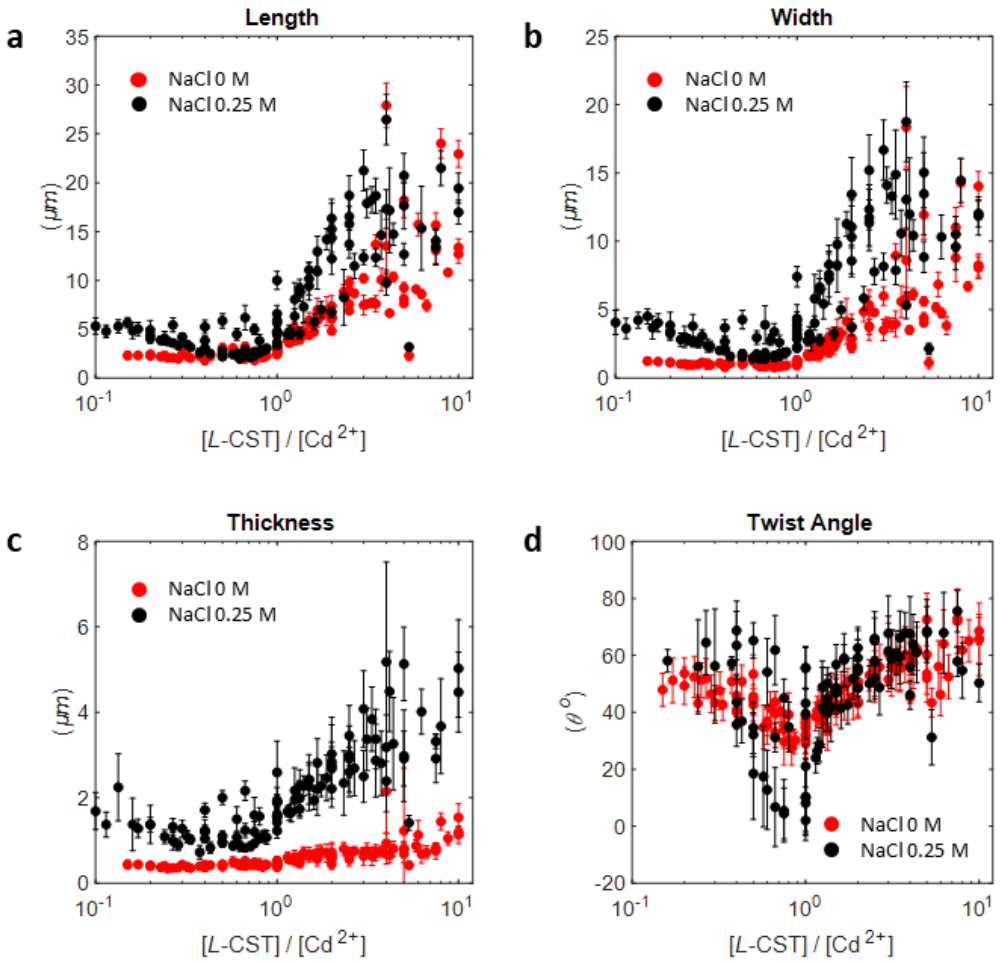

SI Fig 26. Measurements of Length (l), Width (w), Thickness (t) and Twist Angle (θ) of the stack of twisted sheets are plotted with respect to the ratio of [L-CST]/[Cd^{2+}]. Red dots indicate the synthesis conditions without NaCl and blue dots are synthesized in the presence of 0.25 M NaCl. Error bars are calculated from 5-10 measurements of the respective quantity. Note the larger relative increase in thickness for bowties made in 0.25 M NaCl as compared to 0 M NaCl.

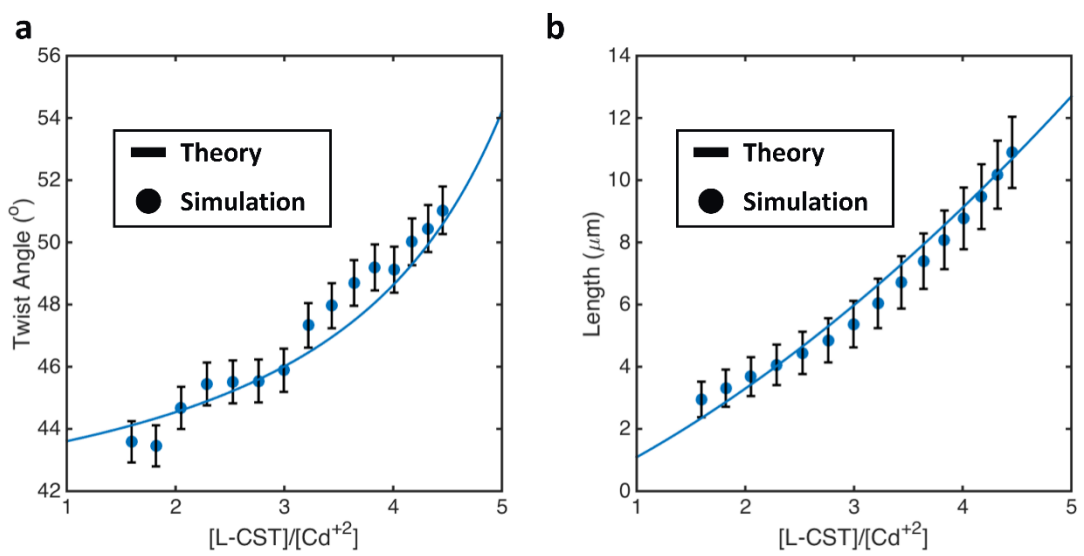

SI Figure 27. Comparison of theory vs Monte Carlo simulations for incomplete cluster formation. a) Twist angle and **b)** Length of bowties. Solid lines are theory predictions. Scatter points are MC growth simulation results.

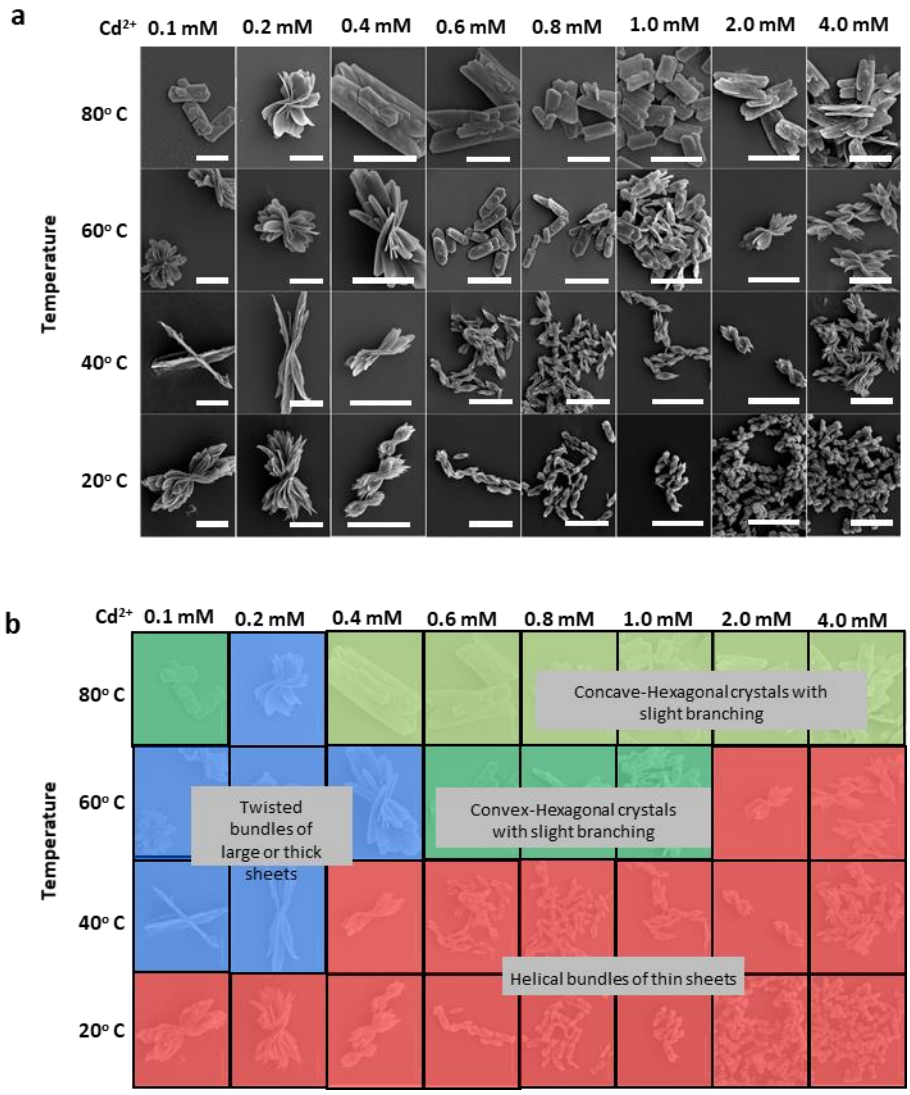

SI Fig 28. Temperature effect on the morphology of Cd_2CST_2 based nanostructured self-assembled particles. a, SEM micrographs of the final bowtie morphology when temperature is varied (along y-axis) from 20-80° C and [*L*-CST]/[Cd^{2+}] ratio is decreased from 8 to 0.2 ([*L*-CST] = 0.8 mM). **b,** The morphologies are classified based on their curvature and stacking patterns. Tracing the y-axis from 20° C to 80° C at a fixed [*L*-CST]/[Cd^{2+}] ratio indicates that the change in stacking and overall sizes. Scale bar in a is 5 μm.

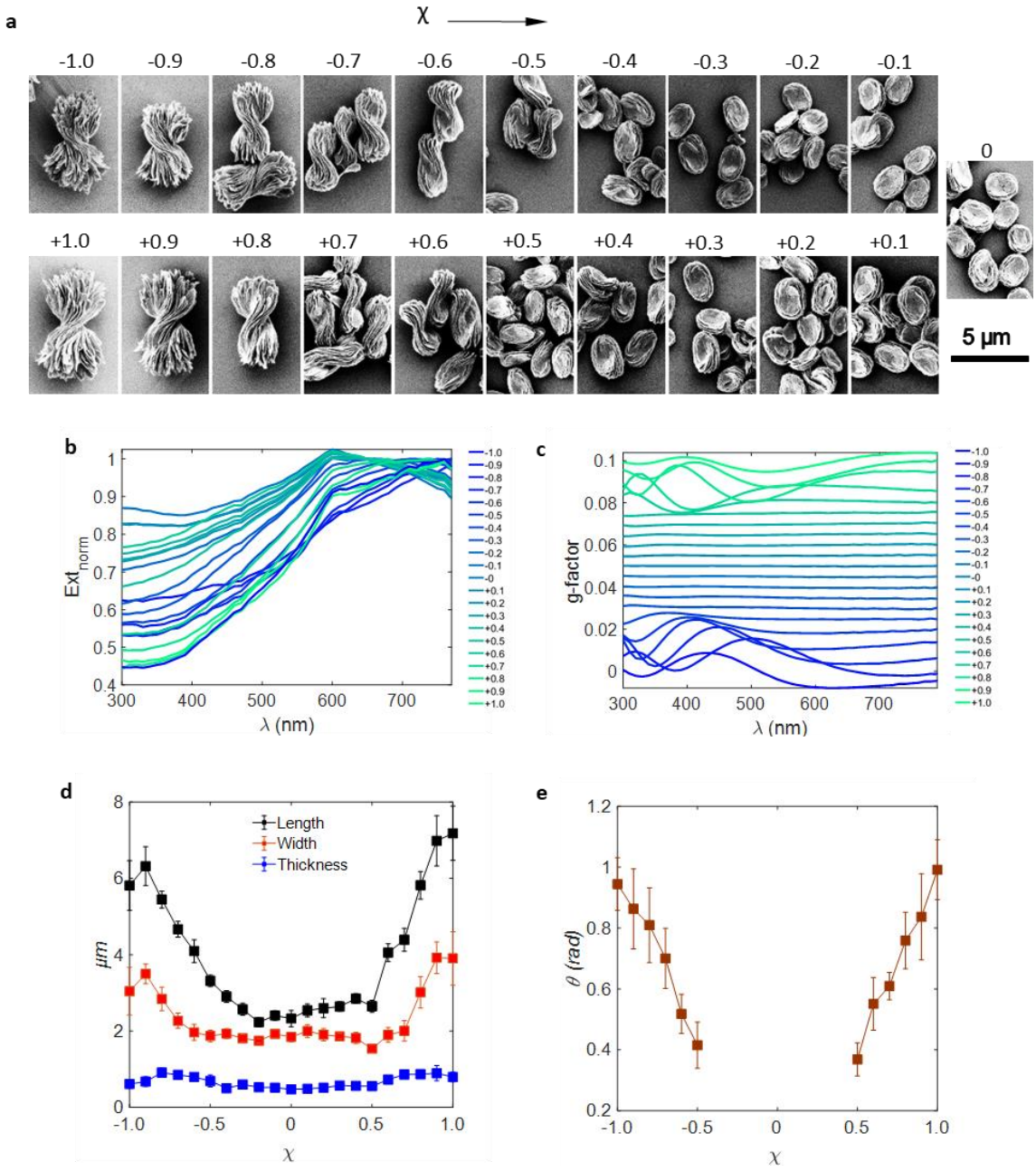

SI Fig 29. Effect of changing the enantiomeric excess. a, SEM images of bowties as enantiomeric excess (χ) defined as ([*L*-CST] – [*D*-CST]) / ([*L*-CST] + [*D*-CST]) is increased from -1 to 1. **b,** corresponding extinction and **c,** g-factor spectra for the morphologies shown above are plotted. **d,** measured morphology parameters of length, width, thickness and **e,** twist angle are plotted. The continuous change of twist angle coupled with a parabolic change in length, width and thickness is a clear indication of the competing mechanical, electrostatic and chemical energy penalties continuously changing with χ.

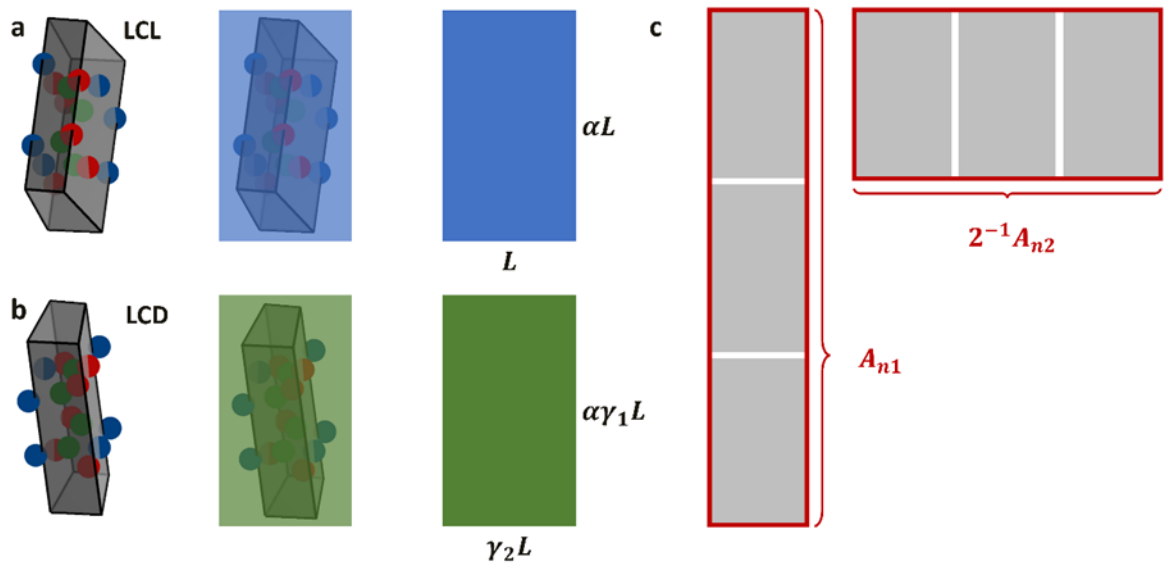

SI Figure 30. Representations of a) LCL and **b)** LCD building blocks. L is the characteristic length of the monomeric building block nanocluster along its long axis, α is the aspect ratio measuring the amount of nanocluster building block elongation, n is the number of nanoclusters in the assembly, and γ_1 and γ_2 are the local curvature of the nanoclusters along the long and short direction, respectively. **c)** Schematic of configurations considered in derivation of A_{n1} and A_{n2}. The 2^{-1} factor accounts for symmetry of the A_{n2} configuration being the same going in the 3rd direction (in/out of page).

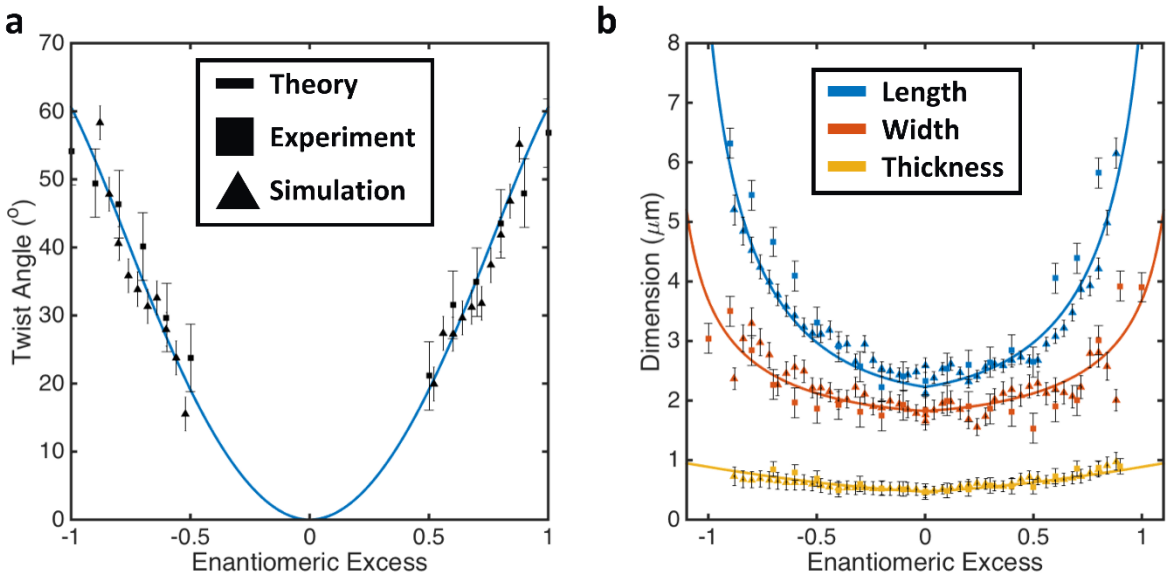

SI Figure 31. Comparison of Various Bowtie Dimensions. Comparison of theory, Monte Carlo growth simulation and experiments for **a)** twist angle and **b)** various bowtie dimensions.

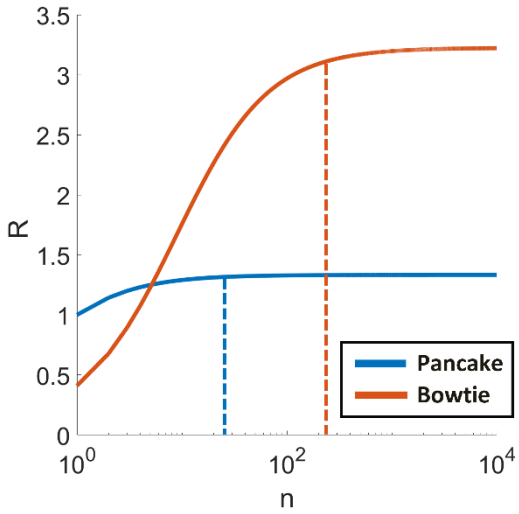

SI Figure 32. Self-Limited Assembly of Bowties. Theoretical prediction of self-limiting sizes (in scaling units) of pancake and bowtie particles as a function number of number of nanoclusters in the particle. Plateau indicates the self-limiting size R^* of the growing particles. Dashed lines indicate the self-limiting number of nanoclusters in the growing particles as predicted from Eq. 11 (i.e. particle stops growing at location of dashed lines).

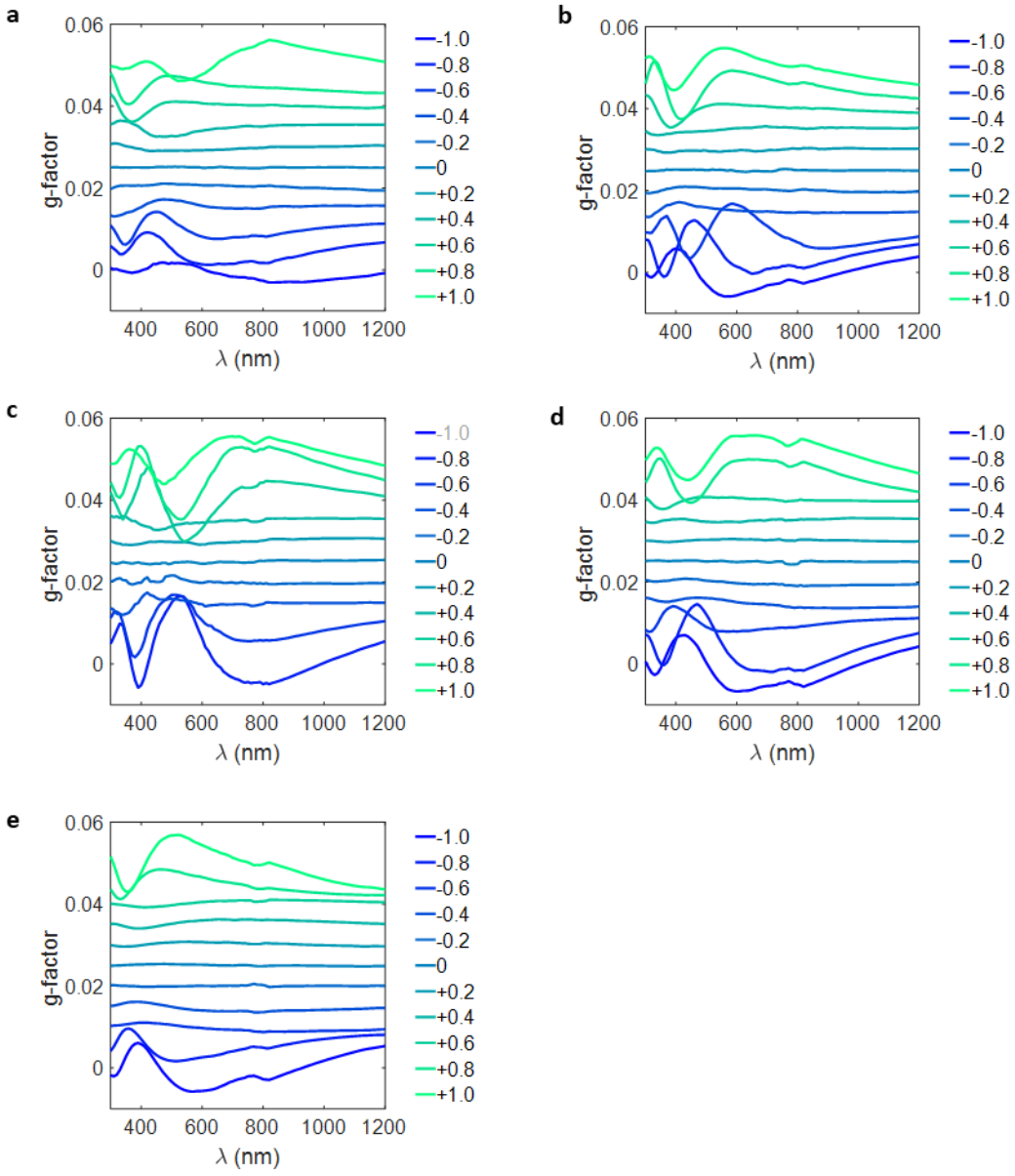

SI Fig. 33. Chiroptical spectra of bowtie particles with different enantiomeric excess. G-factor spectra for bowties with morphologies shown in main text **Fig. 3b** acquired for [Cd^{2+}] equal to **a,** 0.6 mM, **b,** 1.0 mM, **c,** 2.0 mM, **d,** 3.0 mM, **e,** 4.0 mM while maintaining [*L*-CST] = 4 mM.

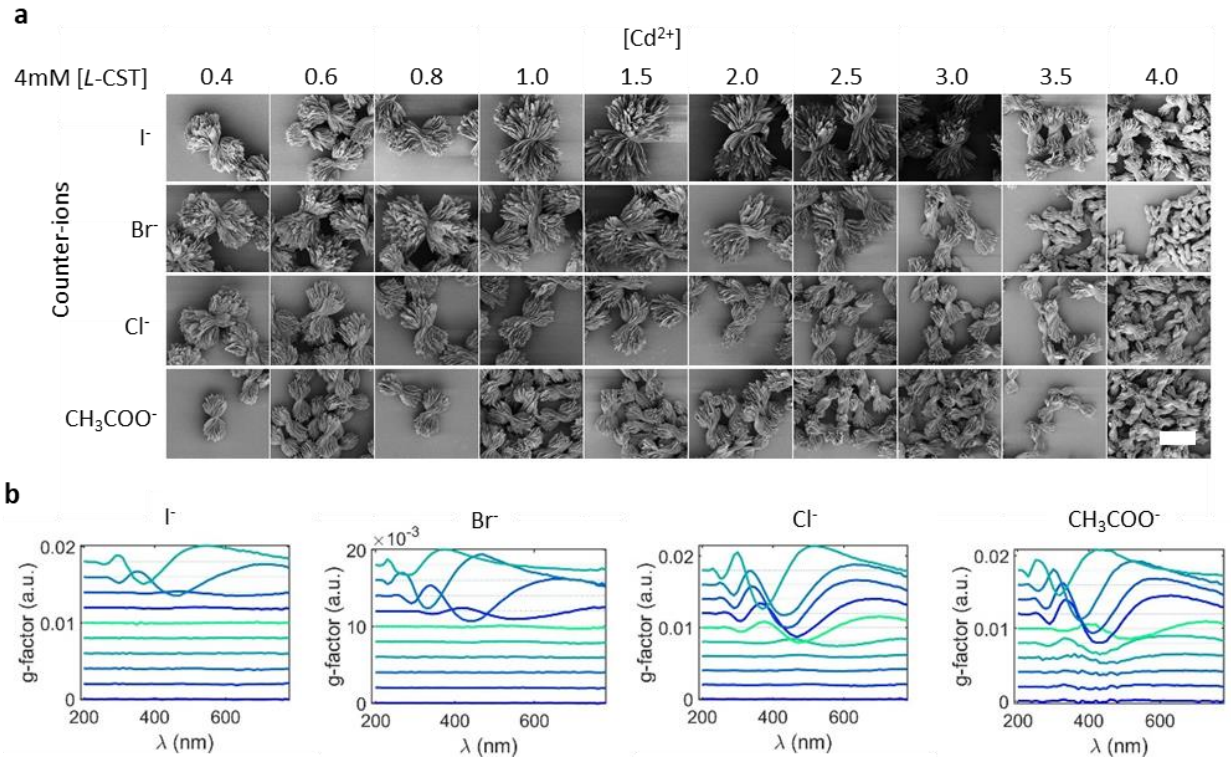

SI Fig 34. Effect of counter-ions on the hierarchical structure of bowties. a, SEM images indicating the changes in the morphology of bowties as the M+/CST ratio is increased for CdI_2. $CdBr_2$, $CdCl_2$, and $Cd(CH_3COO)_2$ as the starting metal salt. Same amount of twist in bowties is produced by different concentration of the metal salt in the following order $[I^-] > [Br^-] > [Cl^-] > [CH_3COO^-]$. This series is in some agreement with the typical Hofmeister series but whether this match is coincidental or significant finding will need to be evaluated further. **b,** Corresponding *g*-factor spectra for the morphologies shown above. Scale bar in (**a)** is 5 μm.

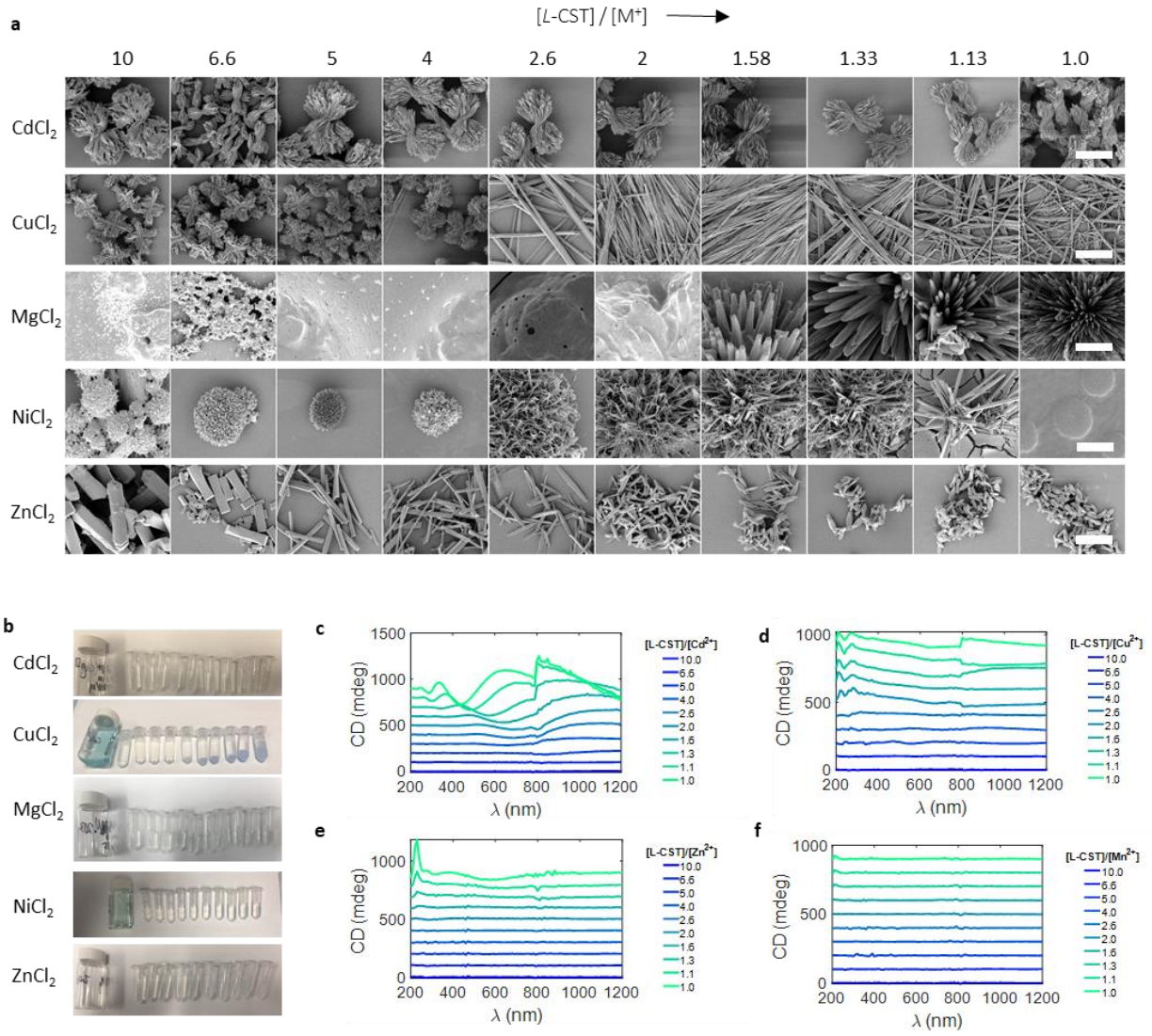

SI Fig 35. Effect of different metal-ions on macroscale morphology. a, Typical morphology of bowtie is shown in the first row which decreases in size as metal ion (M^{+}) concentration increases. Copper shows a cross-stitched assembly of fibers which transitions in to long individual fibers upon increasing metal ion concentration. Mg^{2+} and Ni^{2+} result in spherical supraparticles, while Zn^{2+} results in a rod-like morphology. The pH of CST solution was fixed at 11 while metal ion concentration was increased. These results indicate that different metal ions coordinate in a different manner with the same CST at the molecular level, thereby affecting the overall macroscale morphology. **b,** Photographs of the as prepared samples in centrifuge tubes of 2 ml total volume shown in panel a. Corresponding CD spectra for **c,** Cd^{2+}, **d,** Cu^{2+}, **e,** Zn^{2+}, and **f,** Mg^{2+} are shown here. Scale bar in a is 5 µm.

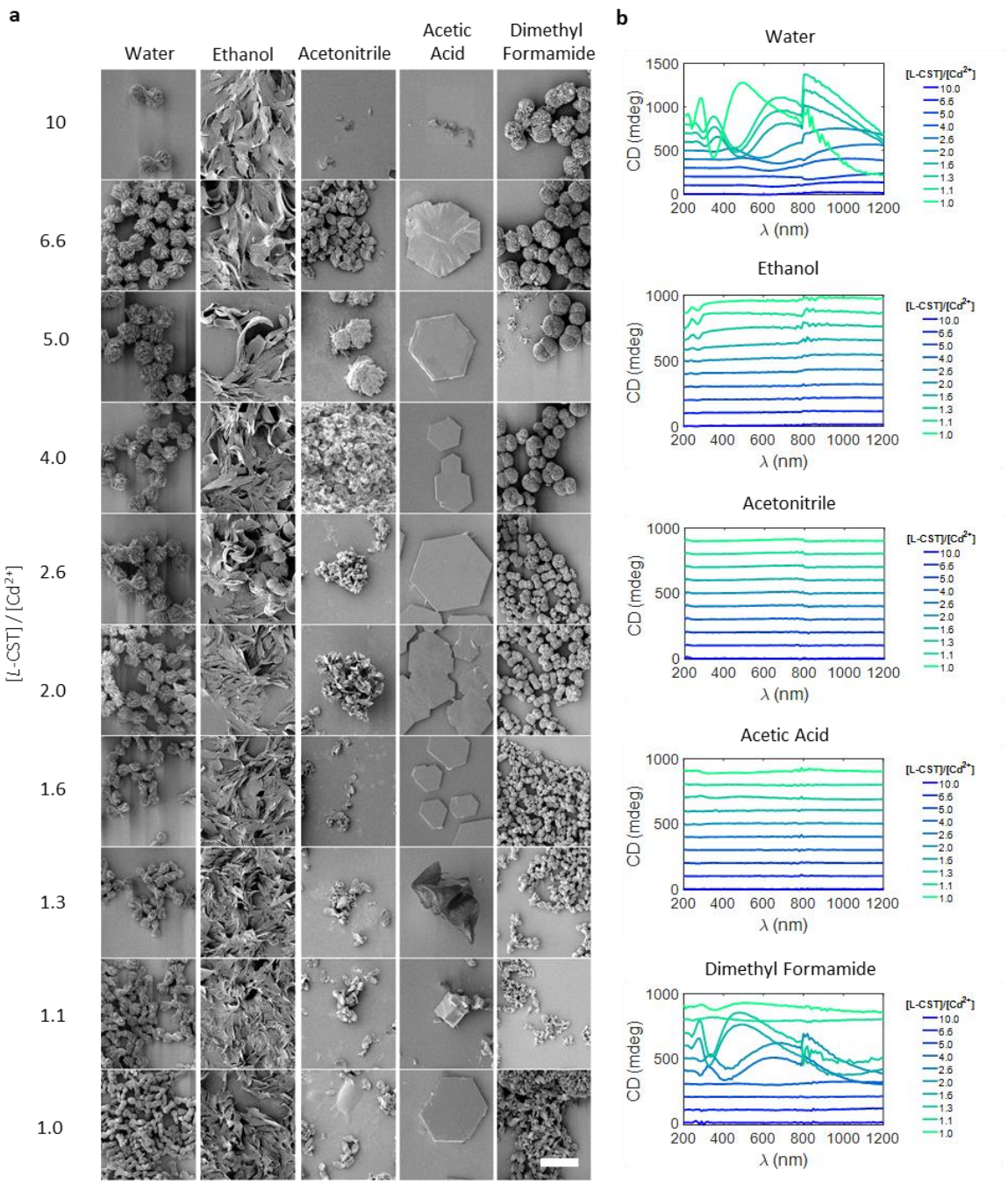

SI Fig 36. Effect of changing the solvent. a, SEM images of bowties self-assembled in 100% by volume of different solvents (x-axis) and the effect of varying [*L*-CST]/[Cd^{2+}] ratio. **b,** Corresponding CD spectra are shown on the right. Scale bar in a is 10 µm.

Note. Solvent affects the interaction between the charged molecules by acting as a screening medium with an effective polarizability and permittivity. This in-turn affects the self-assembly where the transition from stacked bundles in water to individual twisted tapes in ethanol to smaller stacks of twisted bundles in DMF are observed. These morphologies can be further controlled by mixing water and solvent in different ratios.

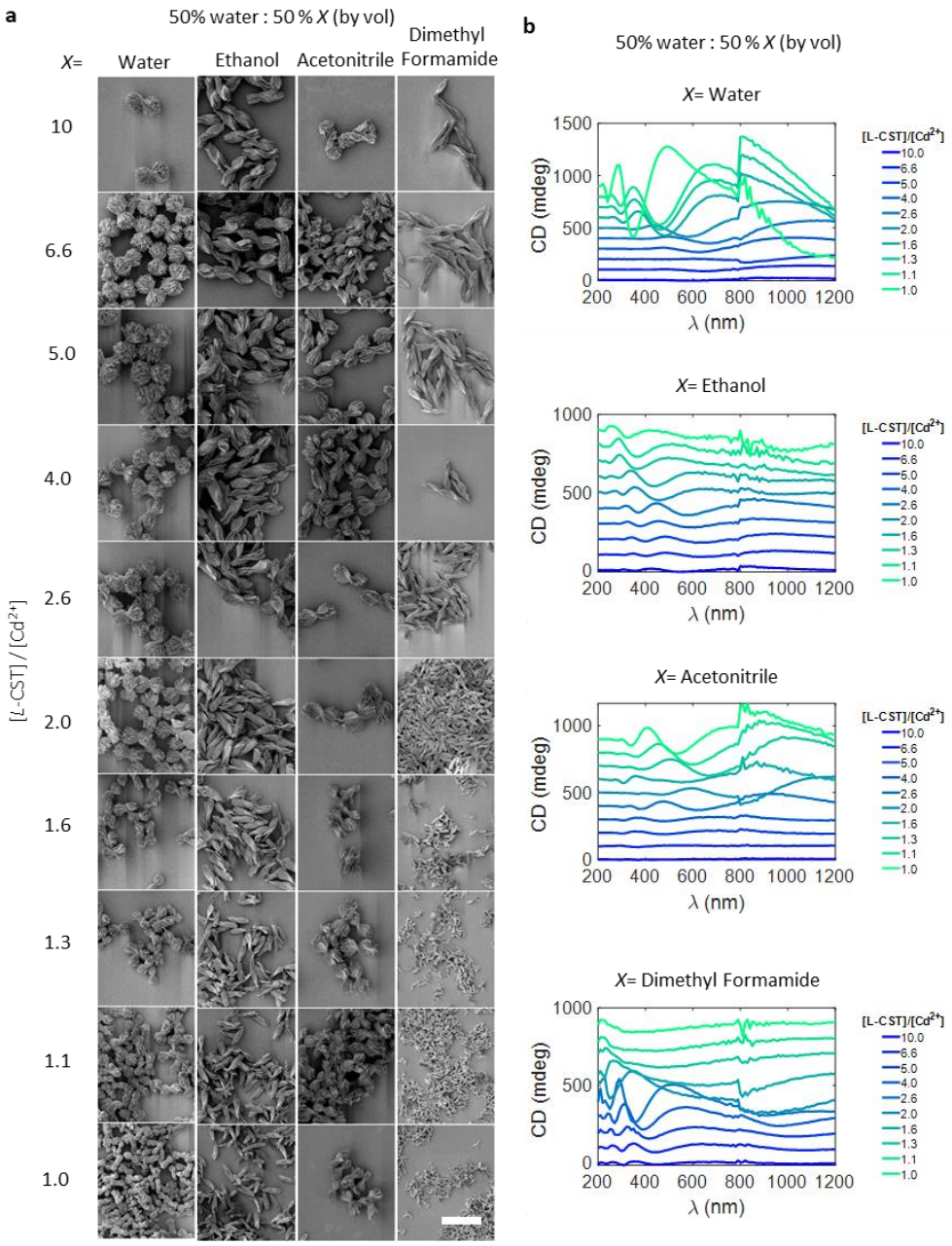

SI Fig 37. Effect of mixing different solvent with water. a, SEM images of the bowties self-assembled in a 50:50 mixture of water and solvents. Changing the solvent along x-axis results in a decrease in stacking thickness, while the overall size decreases along the y-axis as amount of $[Cd^{2+}]$ is increased. **b,** Corresponding CD spectra for the morphologies shown in a is plotted from UV-vis to NIR region. Scale bar in a is 10 µm.

Note. Water-solvent mixtures provide another handle to control the self-assembly pathway of nanoplatelets by changing the interactions between them.

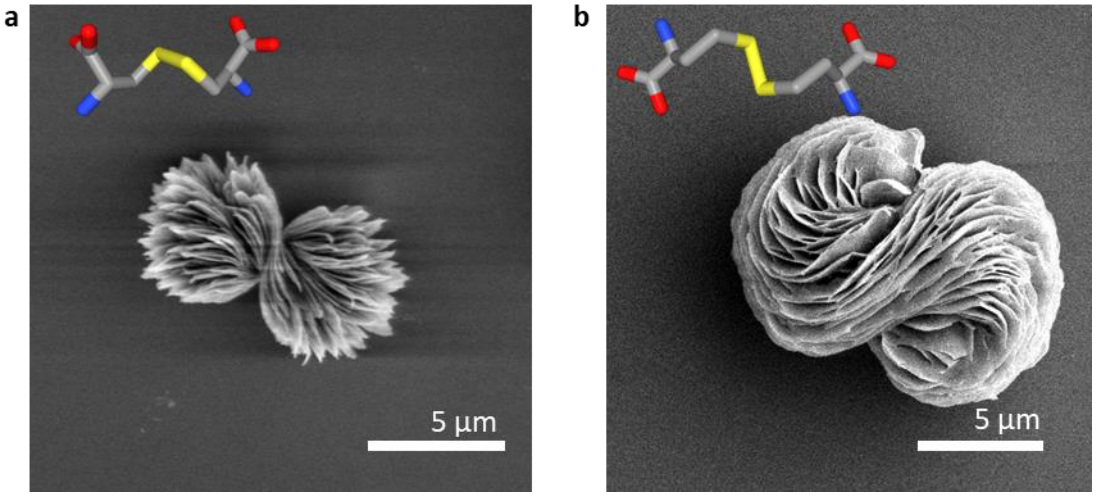

SI Fig 38. Effect of changing the surface ligands in the bowties. SEM image of bowtie made from **a,** *L*-CST and **b,** *L*-homocystine. The twist in the overall morphology increases as the chain length of *L*-CST molecule is increased by two carbon atoms to *L*-homocystine. The stick models of corresponding molecules are overlaid. Note that the reversal in handedness of molecules results in reversal in handedness of the bowtie.

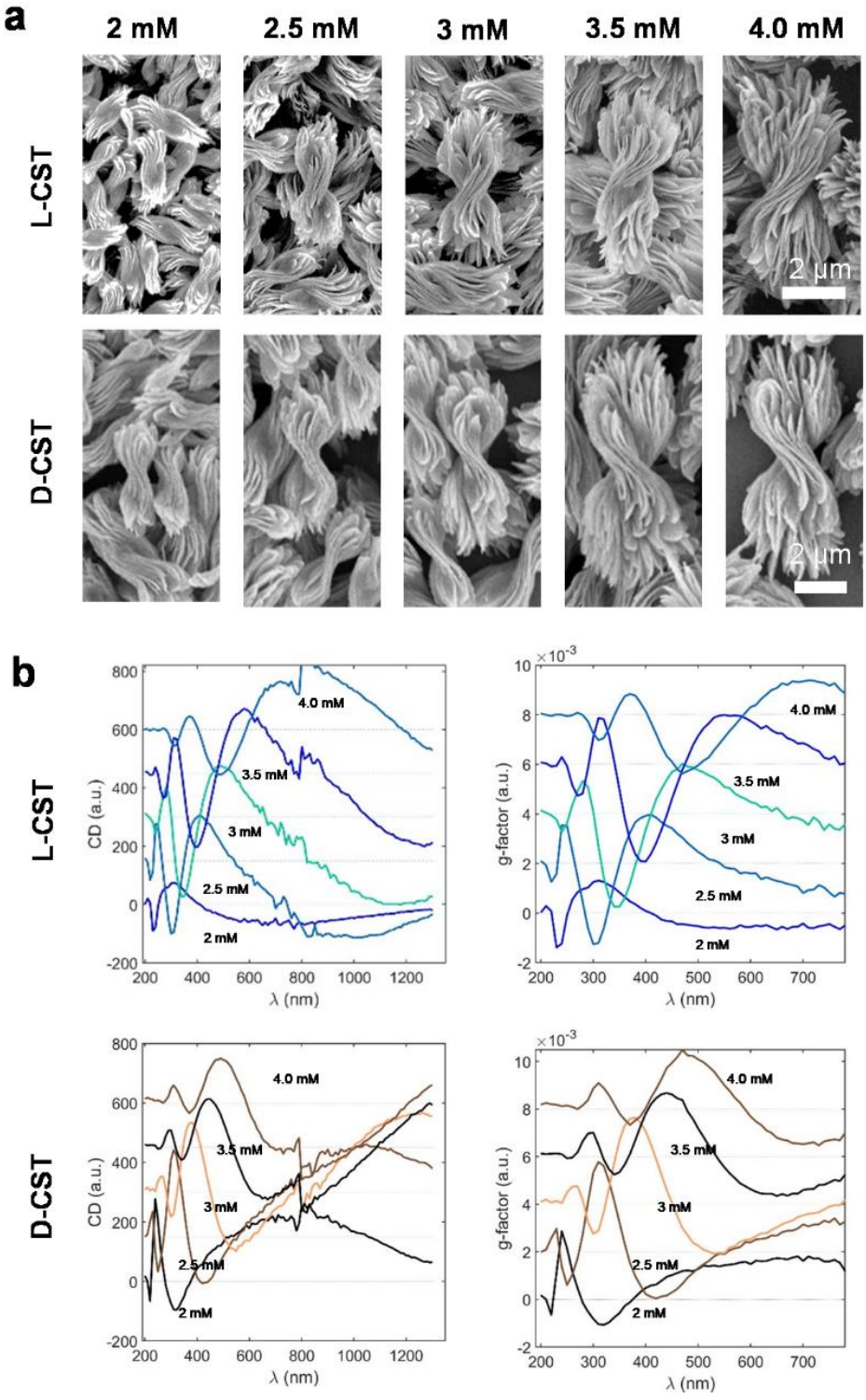

SI Fig 39. Synthesis and optical properties of bowtie particles. . a, SEM images of bowtie assemblies synthesized with [Cd^{2+}] = 2 mM and [*L/D*-CST] = 2 – 4 mM. As [*L*-CST]/[Cd^{2+}] increases the size of bowtie assemblies increases and correspondingly the **b,** CD spectra red shifts.

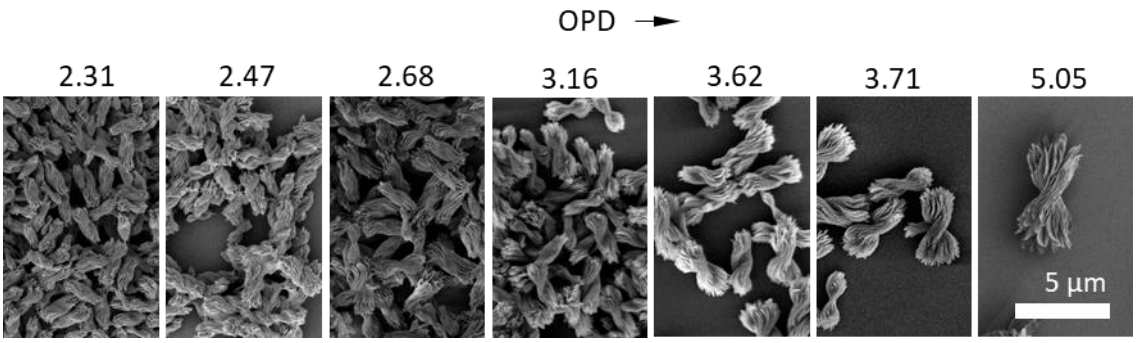

SI fig 40. SEM images and the corresponding OPD indices are shown here for bowties of different sizes for which the *g*-factor spectra is plotted in main text **Fig 4a**.

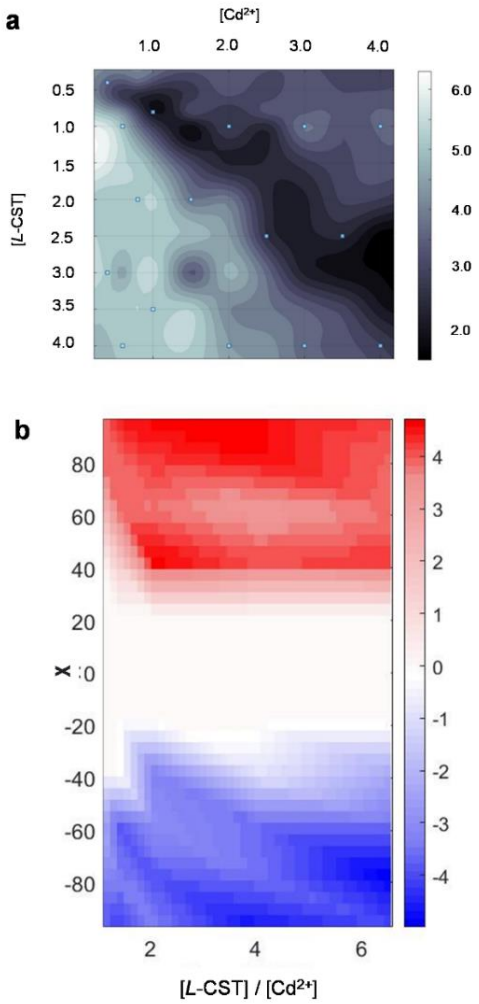

SI Fig 41. Osipov-Pickup-Dunmur chirality measures are plotted for the phase diagrams of **a,** varying [*L*-CST] and [Cd2+] concentrations **b**, Varying enantiomeric excess χ vs. [*L*-CST]/[Cd^{2+}]. Color bars indicate the values of OPDs indices and are positive for panel a and symmetrically opposite in sign for panel b.

Note: Empirical relationship between different morphological parameters and OPD chiral index is as follows –

$$\mathrm{l} = 0.01366\ (OPD)^{3.908} + 1.654, R^2 = 0.6313$$

$$w = 0.0009684\ (OPD)^{5.167} + 0.8329, R^2 = 0.6486$$

$$p = 0.0004143\ (OPD)^{5.69} + 2.657, R^2 = 0.4421$$

$$t = 0.06352\ (OPD)^{1.441} + 0.1806, R^2 = 0.3183$$

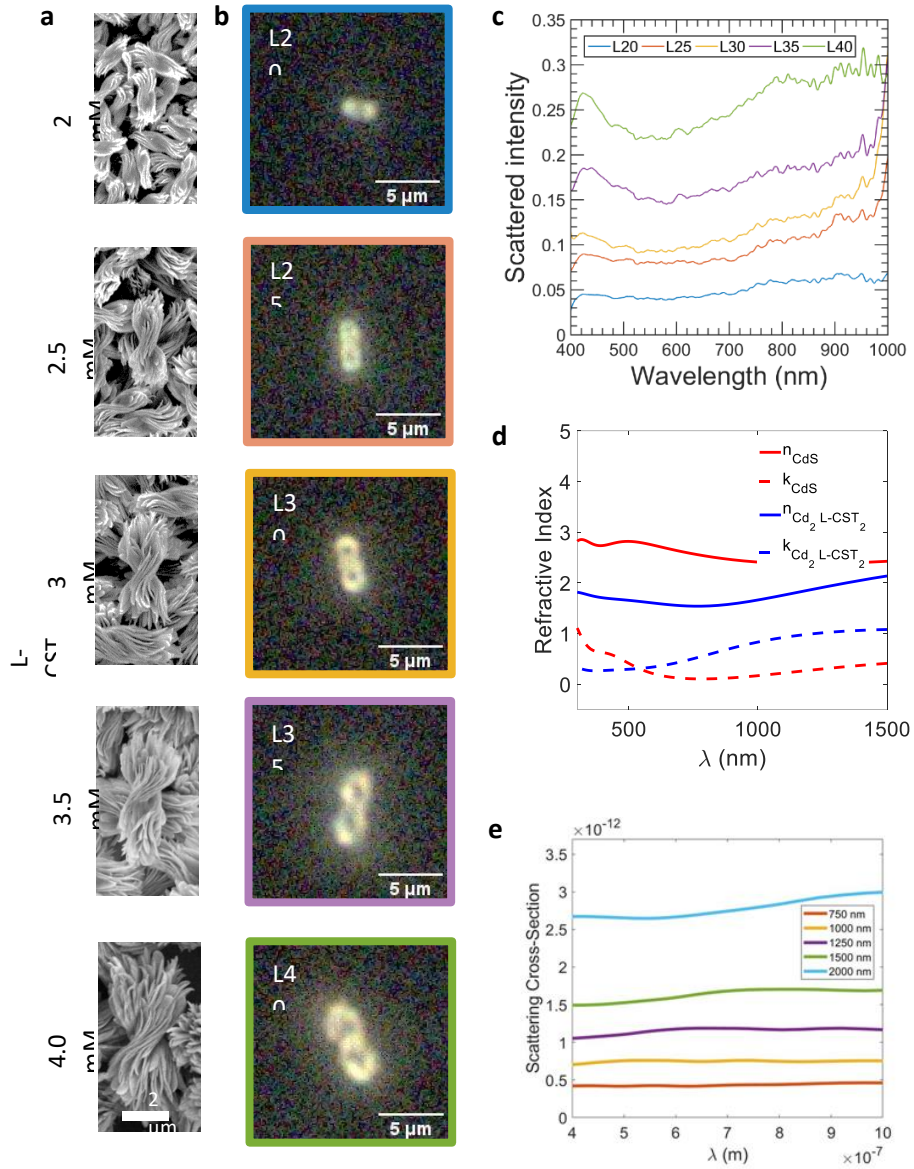

SI Fig 42. Single particle scattering. a, SEM images and **b,** the corresponding optical micrographs of bowties of increasing size. **c,** Scattering intensity spectra upon illumination of bowties with unpolarized light obtained from averaging data from 10 single particles of same size. **d,** Simulated real (*n*) and imaginary part (*k*) of refractive index for CdS and Cd_2(*L*-CST)$_2$. **e,** Simulated scattering cross-section for bowties of increasing sizes obtained as averages of polarized light incident in parallel and perpendicular orientation. The scattering intensity increases as the sizes of bowties increase. Overall the scattering intensity is increased in the NIR regions as compared to visible region upon increase in size of bowties. Above trend is also observed upon simulations of bowties of different sizes.

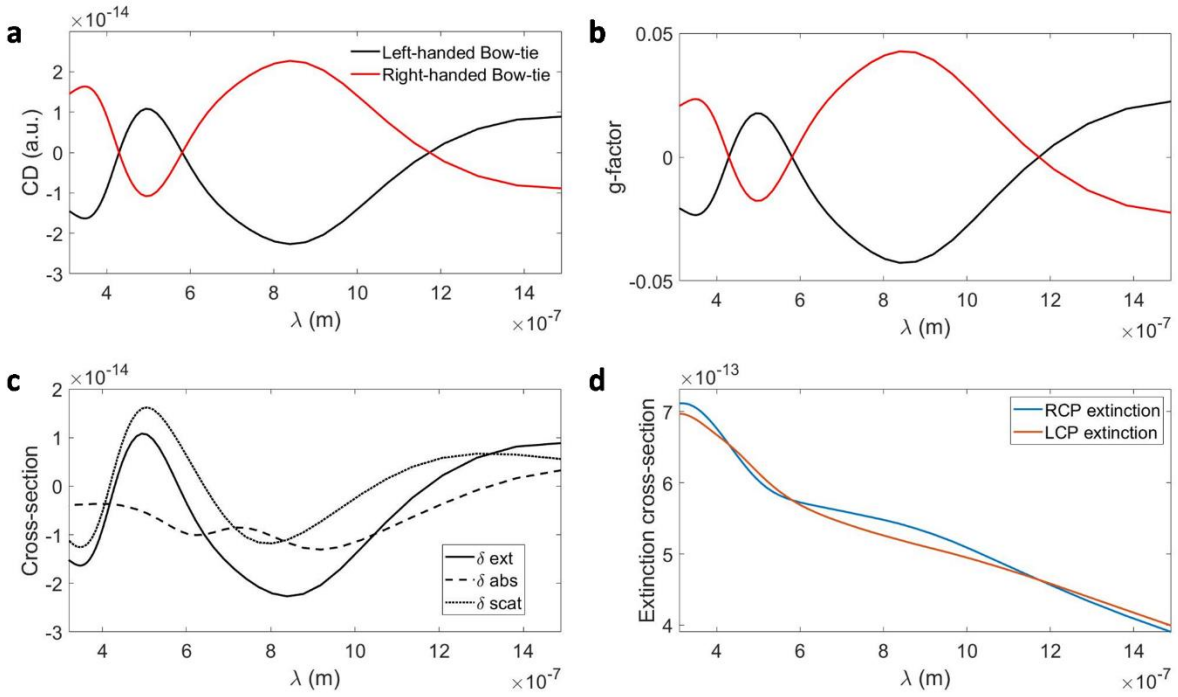

SI Fig 43. Calculated optical properties of bowties with geometry as *l*-1000 nm, *w*-500 nm, *t*-50 nm, *p*-2000 nm. a, CD spectra and **b,** *g*-factor of bowties. **c,** Differential scattering and absorbance contributions to the CD spectra of left-handed bowties. **d,** Extinction cross-section for a left-handed bowtie interacting with LCP and RCP. All the spectra are an average of 100 different orientations to mimic the experimental conditions of a freely rotating bowtie in water.

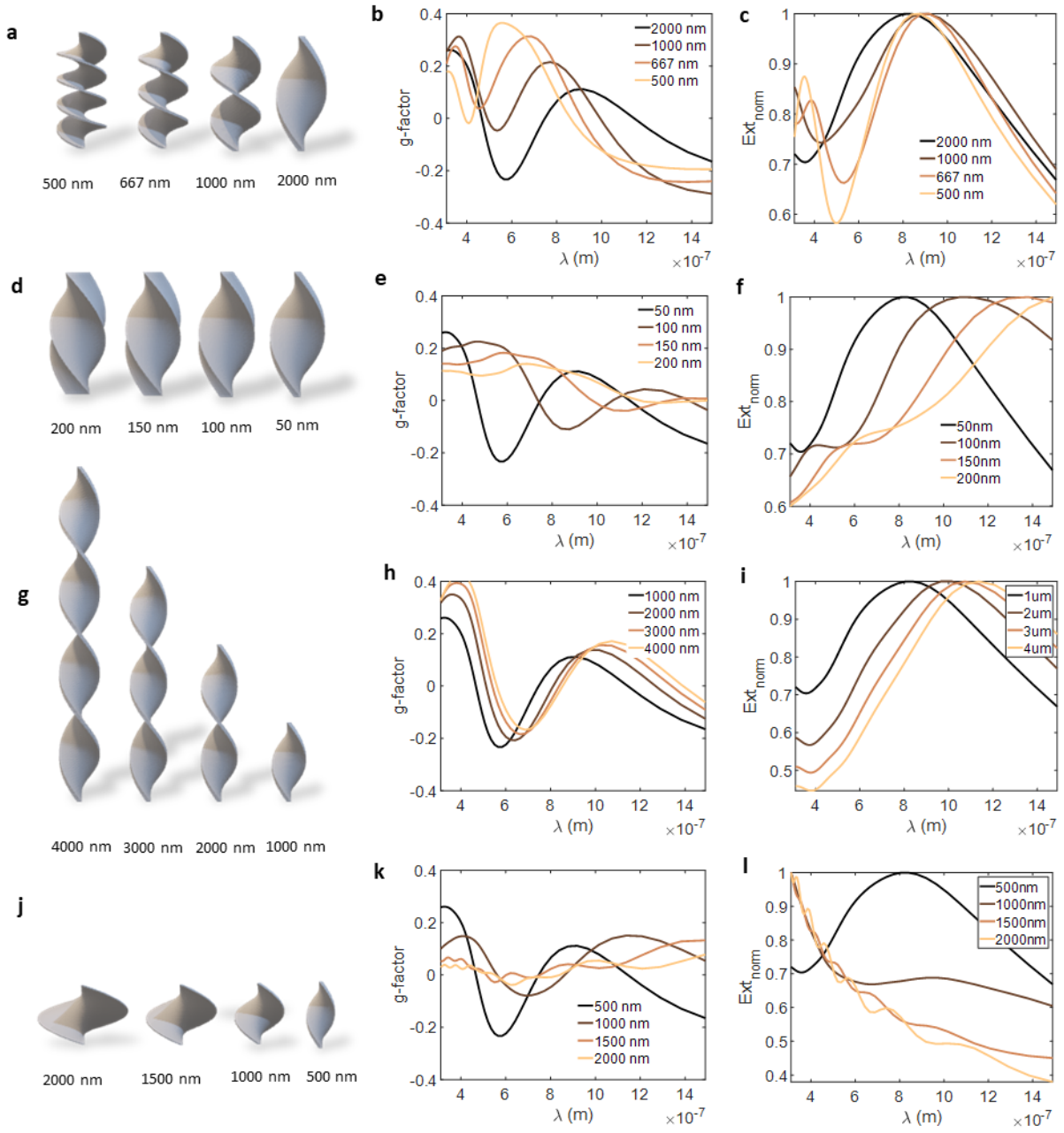

SI Fig 44. Simulated *g*-factor spectra for a twisted left-handed sheet. Modeled geometry and the corresponding *g*-factor and extinction spectra for different **a-c,** pitch, **d-f,** thickness, **g-i,** length, **j-l,** width. Decreasing pitch and thickness blue shifts the spectra, while increasing length and width red shifts the spectra. Modeled geometries are ideal shapes without strong scattering on edges. Hence the *g*-factors are an order of magnitude higher as we observe in experiments.

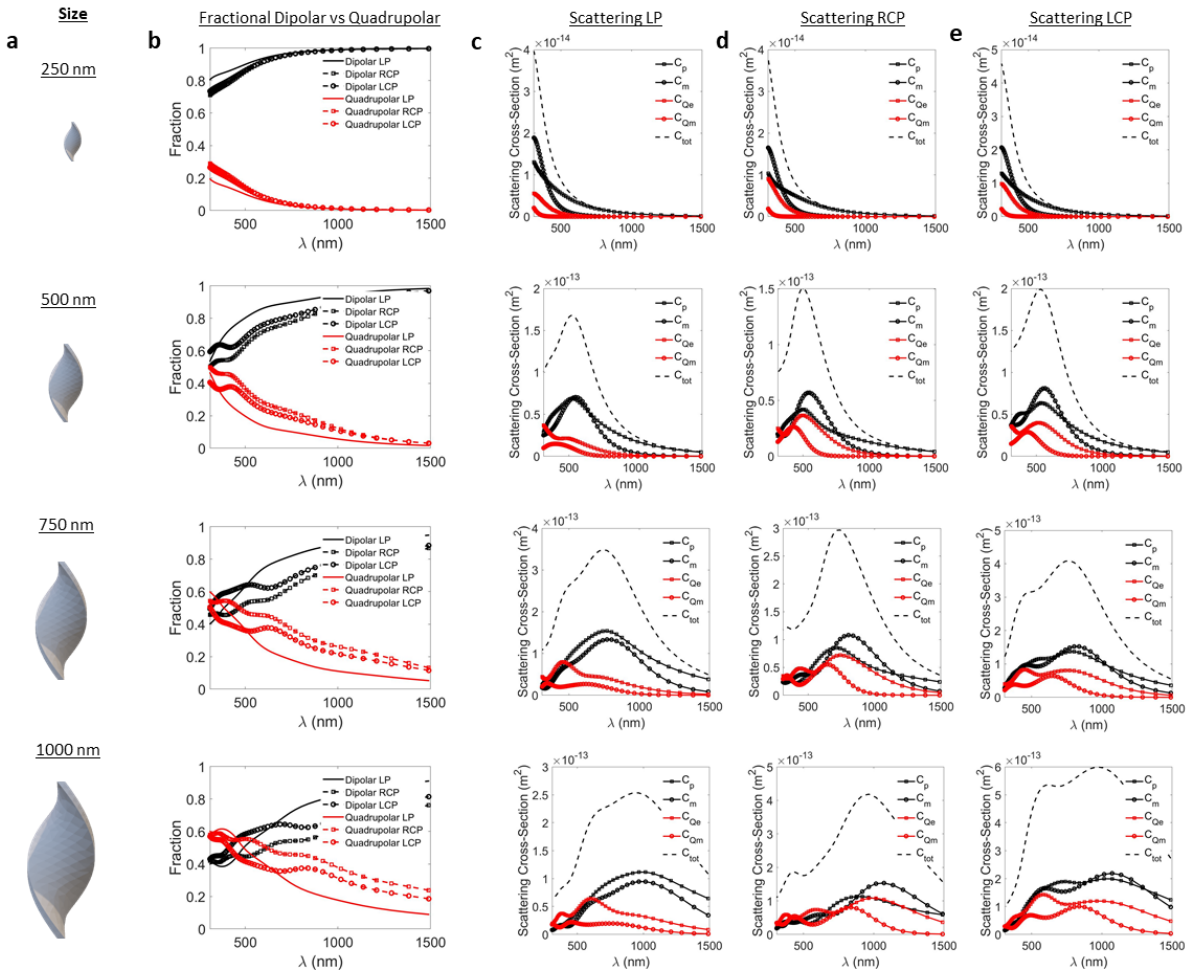

SI Fig 45. Dipolar vs quadrupolar contribution to scattering cross-section. a, (top to bottom) modeled geometry of bowties from length 250 nm to 1000 nm. **b,** fraction of dipolar (electric + magnetic) scattering vs quadrupolar (electric + magnetic) scattering for a left-handed bowtie interacting with linearly polarized (LP) vs right-handed circularly polarized (RCP) vs left-landed circularly polarized (LCP) electromagnetic wave. Total scattering cross-section is decomposed into the constituent electrical (C_p), magnetic (C_m) dipole and electrical (C_{Qe}), magnetic (C_{Qm}) quadrupole scattering cross-sections for **c,** linearly polarized, **d,** Right-circularly polarized (RCP) and **e,** Left-circularly polarized (LCP) electromagnetic wave.

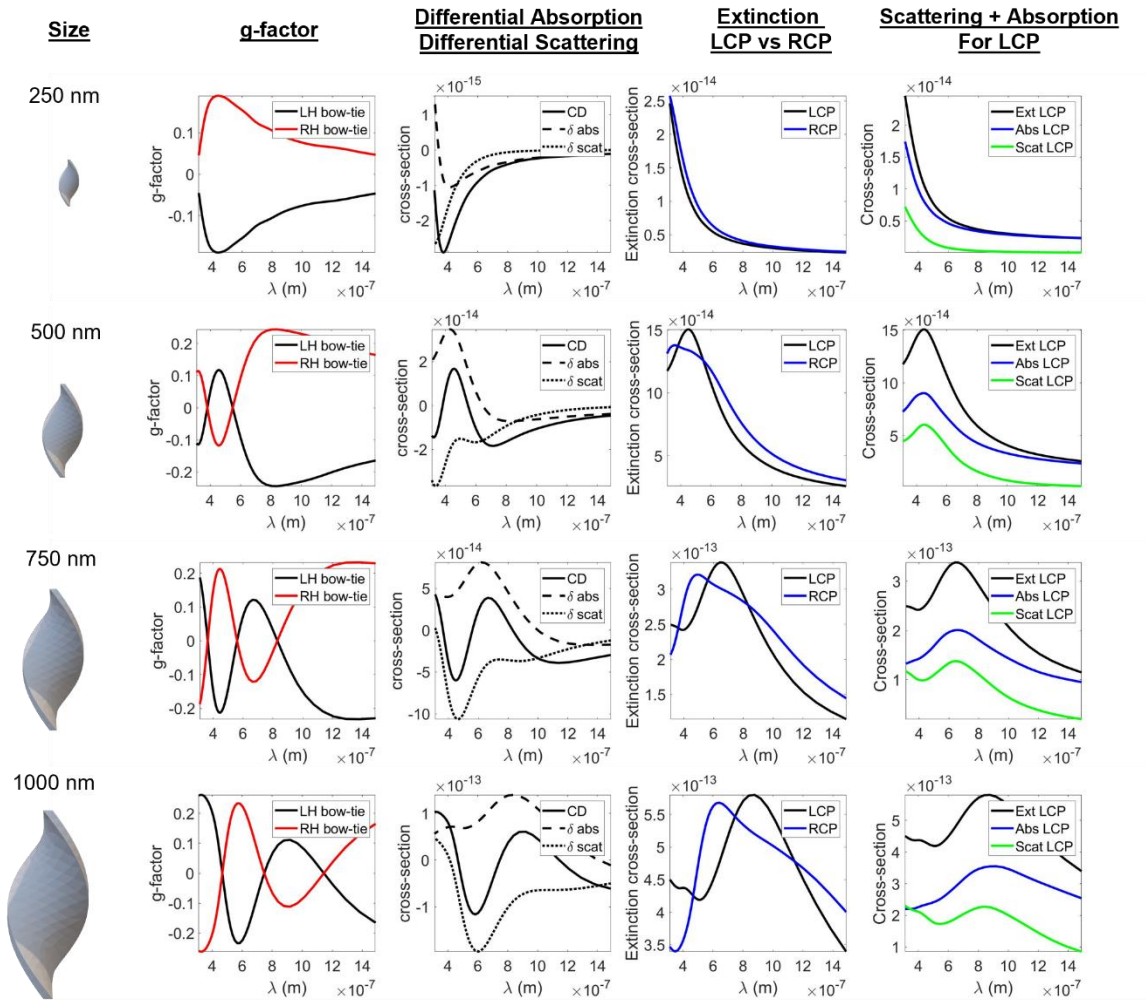

SI Fig 46. Models for bowtie with variable size. a, Upon scaling the size of the bowtie from 250 nm to 1000 nm, the width, length, thickness and pitch increase simultaneously as shown here. **b,** the maximum *g*-factor spectra red-shifts from 400 nm to 800 nm to 1200 nm as the size increases from 250 nm to 1000 nm. **c,** Correspondingly the differential absorption peaks at the same wavelength as the size of the bowtie, while the differential scattering of the bowtie peaks at slightly smaller wavelengths as compared to absorption. **d,** Extinction spectra for the left-handed twisted sheet upon interaction with LCP and RCP. **e,** Contribution from absorption and scattering to extinction cross-section when LCP interacts with a left-handed twisted sheet.

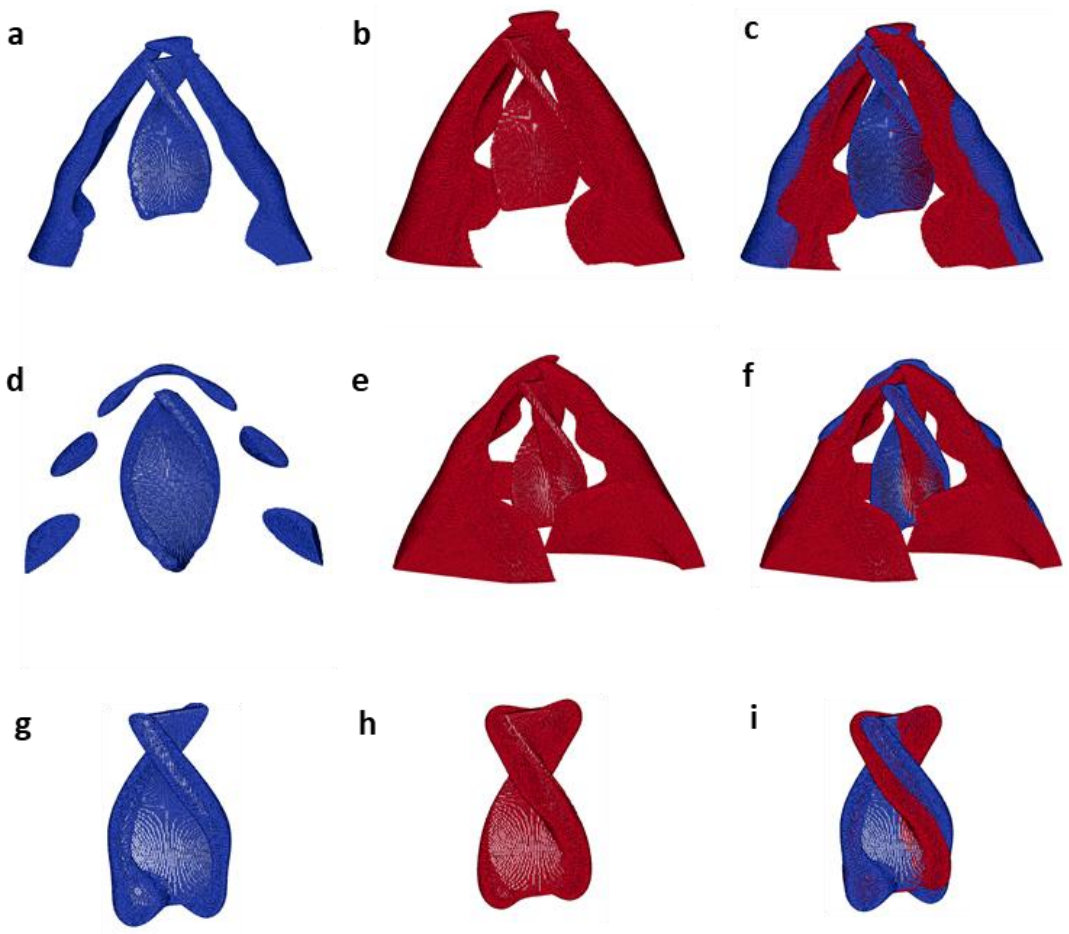

SI fig 47. Scattered electromagnetic field around bowties. The field with the isoline at 2.5 $(V/m)^2$ is plotted around a left-handed twisted sheet model with a length of 1000 nm for **a,d,g** RCP (blue) **b,e,f** LCP (red) of wavelength **a,b,** 385 nm, **d,e,** 550 nm, **g,h,** 1137 nm. The scattered field from LCP and RCP are overlaid in panels **c,f,i**. At 385 nm differential scattered field is zero, at 550 nm it is maximum and at 1137 nm it is a local maximum. Note that the LCP scattered field (red) extends to farther regions in space than the RCP. At higher wavelengths the scattered field is dipolar in nature as seen from the single twisted lobe around the surface of the twisted sheet, while at lower wavelengths it is quadrupolar in nature as seen from two perpendicular lobes emanating from the top in panels **a-f**. See **Video S3, S4** for fields distributions in wavelength range of 300-1500 nm. Stronger coupling of LCP with LH sheet causes the scattering to be intense and continuous as compared to mismatch in handedness.

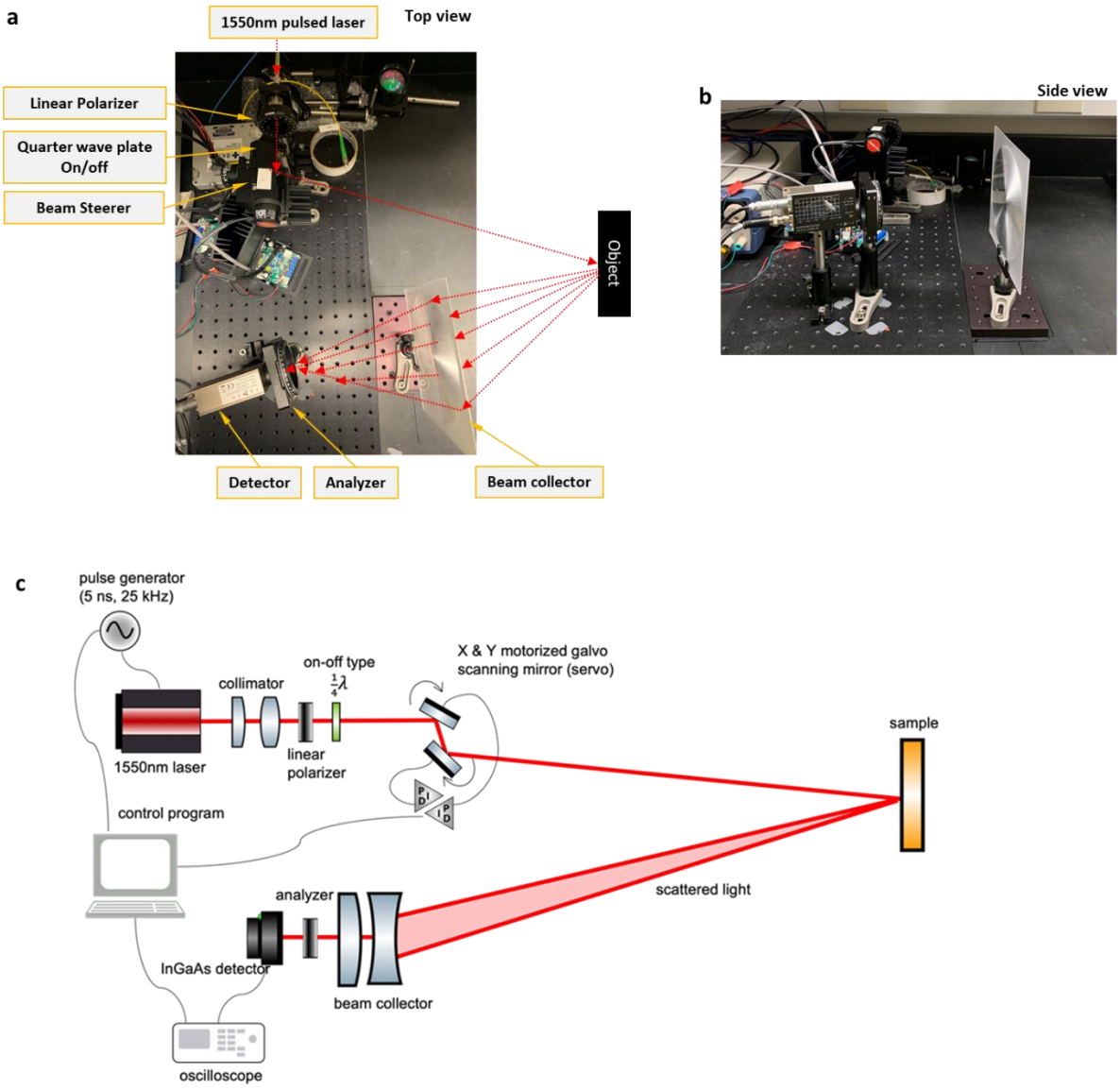

SI Fig 48. Polarization LIDAR setup for testing printed metasurfaces from bowties. Photographs of the optical arrangement for measuring the scattered rays from the bowtie coatings as seen from the **a,** top and **b,** side. **c,** Schematic of the polarization LIDAR setup with 1550 nm laser.

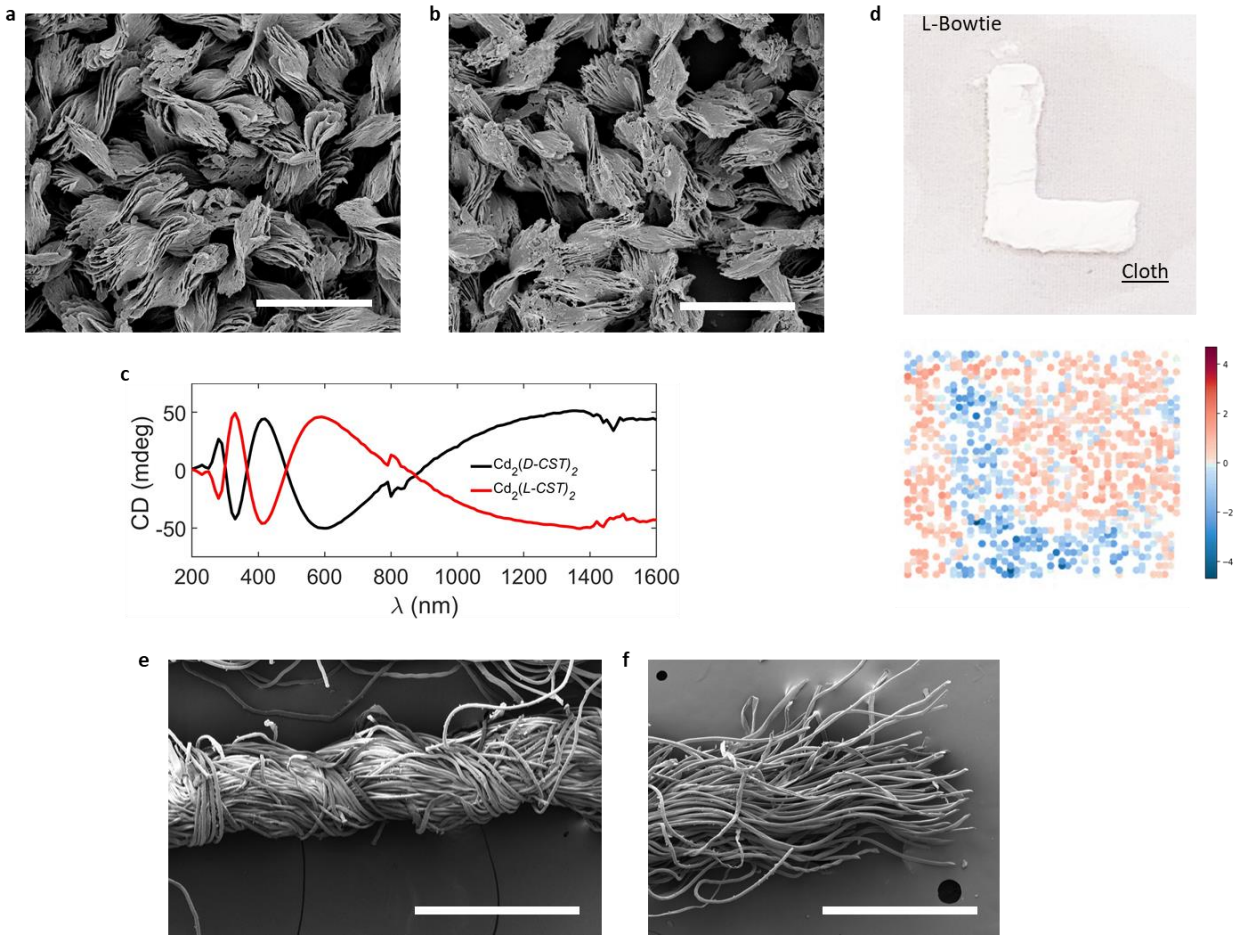

SI Fig 49. Bowties utilized in for printed metasurfaces tested by LIDAR with 1550 nm laser. SEM image of **a,** Cd_2(*D*-CST)$_2$ and **b,** Cd_2(*L*-CST)$_2$ bowties. **c,** CD spectra for the samples shown in panels **a** and **b**. **d,** Printed layer of *L*-bowtie dispersed in PAA on cloth and the corresponding circular dichroism LIDAR backscattered signal of 1550 nm wavelength. SEM image of **e,** fibers of cloth bundled together and **f,** individual fibers. Scale bars are in **a,b** are 5 μm and in **e,f** are 500 nm.

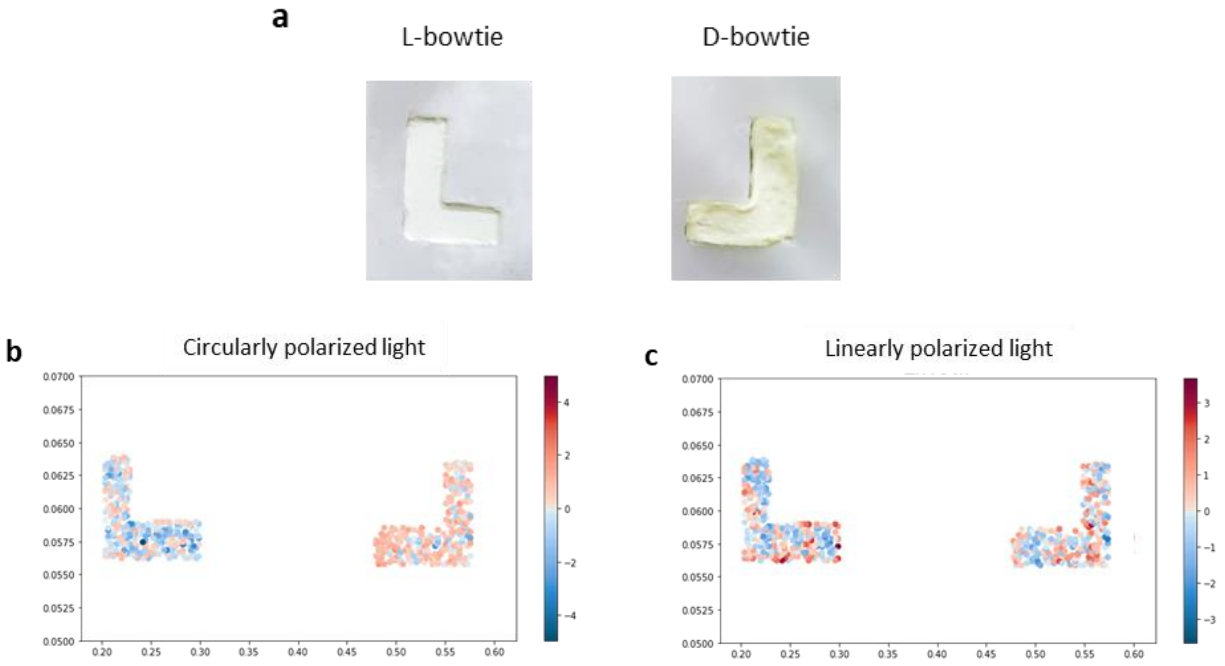

SI Fig 50. Comparison of LIDAR backscattered signal under circularly polarized light and linearly polarized light. a, Printed segment of *L*- and *D*-bowties on glass. **b,c,** The corresponding LIDAR backscattered signal at 1550 nm for **b,** circular dichroism and **c,** linear dichroism. There is little difference when LIDAR beam is linearly polarized.

SI REFERENCES

(1) Toby, B. H.; Von Dreele, R. B. GSAS-II: The Genesis of a Modern Open-Source All Purpose Crystallography Software Package. *J. Appl. Crystallogr.* **2013**, *46* (2), 544–549. https://doi.org/10.1107/S0021889813003531.

(2) Osipov, M. A.; Pickup, B. T.; Dunmur, D. A. A New Twist to Molecular Chirality: Intrinsic Chirality Indices. *Molec. Phys.* **1995**, *84* (August), 1193–1206. https://doi.org/10.1080/00268979500100831.

(3) Kim, J.-Y.; Yeom, J.; Zhao, G.; Calcaterra, H.; Munn, J.; Zhang, P.; Kotov, N. Assembly of Gold Nanoparticles into Chiral Superstructures Driven by Circularly Polarized Light. *J. Am. Chem. Soc.* **2019**, *141* (30), 11739–11744. https://doi.org/10.1021/jacs.9b00700.

(4) Pettersen, E. F.; Goddard, T. D.; Huang, C. C.; Couch, G. S.; Greenblatt, D. M.; Meng, E. C.; Ferrin, T. E. UCSF Chimera--a Visualization System for Exploratory Research and Analysis. *J. Comput. Chem.* **2004**, *25* (13), 1605–1612. https://doi.org/10.1002/jcc.20084.

(5) Kim, J.-Y.; Yeom, J.; Zhao, G.; Calcaterra, H.; Munn, J.; Zhang, P.; Kotov, N. Assembly of Gold Nanoparticles into Chiral Superstructures Driven by Circularly Polarized Light. *J. Am. Chem. Soc.* **2019**, *141* (30). https://doi.org/10.1021/jacs.9b00700.

(6) Pettersen, E. F.; Goddard, T. D.; Huang, C. C.; Couch, G. S.; Greenblatt, D. M.; Meng, E. C.; Ferrin, T. E. UCSF Chimera--a Visualization System for Exploratory Research and Analysis. *J. Comput. Chem.* **2004**, *25* (13), 1605–1612. https://doi.org/10.1002/jcc.20084.